UNIVERSIDADE D
COIMBRA

Beatriz da Costa Lopes Pinto

DEVELOPMENT OF MULTIFUNCTIONAL COATINGS FOR THE NAVAL INDUSTRY

Dissertação no âmbito do Mestrado em Engenharia Mecânica no ramo de Produção e Projeto orientada pela Professora Doutora Sandra Carvalho e pelo Mestre José David Castro, apresentada ao Departamento de Engenharia Mecânica da Faculdade de Ciências e Tecnologia da Universidade de Coimbra.

Julho de 2022

1 2 9 0

FACULDADE DE CIÊNCIAS E TECNOLOGIA
UNIVERSIDADE D COIMBRA

Development of multifunctional coatings for the naval industry

Submitted in Partial Fulfilment of the Requirements for the Degree of Master in Mechanical Engineering in the speciality of Production and Project

Desenvolvimento de revestimentos multifuncionais para a indústria naval

Author

Beatriz da Costa Lopes Pinto

Advisor[s]

Sandra Maria Fernandes Carvalho

José David Castro

Jury

President	**Professora Doutora Ana Sofia Figueira Ramos** **Professora Auxiliar da Universidade de Coimbra**
Vowel[s]	**Professor Doutor Ricardo Gil Henriques Serra** **Investigador Doutorado da Universidade de Coimbra**
Advisor	**Professora Doutora Sandra Maria Fernandes Carvalho** **Professora Associada da Universidade de Coimbra**

Coimbra, July 2022

À minha família,

A Coimbra.

ACKNOWLEDGEMENTS

I would like to thank both my advisors, José David Castro and Sandra Carvalho, for all the time displayed to teach and help me, and for giving me the opportunity to develop this work. To all my teachers and employees of the Mechanical Engineering Department, that always treated me with much care.

To my parents, for all the support they always gave me, the amazing education and strength they always passed me, and for the pride always shown during this chapter. To my sister, for being always there for me even though she's far, for giving me the best examples and always cheering for my success. To all my friends that accompanied me during these academic and non-academic years for all the love, companionship and support they always showed me. A special acknowledgment to Sara, Bea Menezes, David, Jorge, Duarte, Marta, Joana, Afonso, Rita, Daniel, Bea, Besuga, for the close friendship we kept along the years. To my oldest friend Maria, that always supported me and shared with me the greatest accomplishments. To all my colleagues from the swimming section, I appreciate the amazing bond we created.

To all the teams of NEEMAAC that I've crossed, which provided me such important skills but most importantly, amazing friends. A special thank you to Gabriela, Areal, Afonso, Diogo, Jobe, Curado, and everyone else that crossed my paths in those amazing 3 years.

The greatest accomplishments are always better if the people we love are there to share them with.

Abstract

The naval industry, responsible for maritime transport, represents a major weight in the worldwide economy, thus, it is crucial to preserve its structures for the longest time possible, avoiding constant maintenance interventions. The marine environment is known to be very aggressive being an extreme corrosive environment, mainly for sea chest gratings and filters. Moreover, these structures catch micro-organisms that get attached and accumulate in the gratings, getting dragged into other marine habitats and harming the fauna and flora of the sea. This phenomenon is defined as biofouling. Indeed corrosion, common in metals exposed to sweater and, together with biofouling, provoke important increasing in maintenance time stops and hence, a rise in the operation costs.

With this concern, the present work involved the study and development of anticorrosive coatings that would be the baseline for an anti-biofouling coating, that would protect the sea chest gratings from corrosive agents and biofouling. This base coating, formed by zirconium nitride (ZrN), was expected to have good mechanical properties such as hardness and adhesion strength, and on the other hand, good corrosion resistance influenced by the chemical, physical and structural properties.

The development of the ZrN coatings was performed by reactive magnetron sputtering (MS) technology, a Physical Vapor Deposition (PVD) technique. Two different power sources were applied to obtain the films through this technology. Direct Current (DCMS) and High-Power Impulse (HiPIMS – DOMS). The use of HiPIMS improved, in general, the morphological quality of the films, mechanical and anticorrosive properties, by the deposition of films with a dense morphology, low surface roughness, hydrophobicity and low corrosion rates, although having lower deposition rates. It was concluded that films deposited by HiPIMS with high nitrogen content, present a good protection against corrosion, as well as an improvement in general terms of all properties when compared to the uncoated SS 316L substrate.

Keywords: Coatings, Corrosion, Sputtering, Films, HiPIMS, DCMS.

Resumo

A indústria naval, responsável pelo transporte marítimo de produtos, representa uma grande importância na economia mundial e, desta forma, é crucial preservar as suas estruturas durante o máximo período de tempo, evitando constantes intervenções de manutenção. O ambiente marinho é bastante agressivo, pelo facto de ser extramente corrosivo, especialmente em grades e filtros de aço. Estas estruturas capturam micro-organismos que se vão acumulando, sendo arrastados para outros habitats marinhos, prejudicando a fauna e flora do oceano. Este fenómeno é definido como o *biofouling*. De facto, a corrosão, comum em metais que são expostos ao ambiente marinho e, em conjunto com o biofouling, provoca o aumento de paragens para manutenção e, consequentemente, aumento nos custos de operação.

Com esta preocupação, o presente trabalho envolveu o estudo e desenvolvimento de revestimentos anticorrosivos que irão ser a base para um revestimento com atividade antimicrobiana, que irá proteger as grades de agentes corrosivos e organismos que causam *biofouling*. Este revestimento base, constituído por nitreto de zircónio (ZrN), deve ter boas propriedades mecânicas tais como dureza e força de adesão e, por outro lado, boa resistência à corrosão que é influenciada pelas propriedades químicas, físicas e estruturais.

O desenvolvimento dos revestimentos de ZrN foi feito através de pulverização catódica em magnetrão, uma técnica de Deposição Física por Vapor. Foram utilizadas duas fontes de energia para obter os filmes através desta tecnologia. Fonte de corrente direta (*DCMS*) e fonte de alta potência pulsada (*HiPIMS* - *DOMS*). Foi concluído que o uso de *HiPIMS* melhorou bastante as qualidades morfológicas dos filmes, assim como as propriedades mecânicas e corrosivas, através da deposição de filmes com uma morfologia densa, superfícies com baixa rugosidade, superfícies hidrofóbicas e baixas taxas de corrosão, apesar das baixas taxas de deposição. Especialmente os filmes depositados por *HiPIMS* e com alta percentagem de azoto constituíram uma boa proteção contra a corrosão, assim como uma melhoria geral nas propriedades quando comparado com o substrato sem revestimento.

Palavras-chave: Revestimento, Corrosão, Pulverização catódica, Filmes, HiPIMS, DCMS.

Contents

LIST OF FIGURES

LIST OF TABLES

LIST OF SIMBOLS AND ACRONYMS/ ABBREVIATIONS

List of Symbols

σ_f – residual stresses

E_s – Young's modulus

h_s – substrate thickness

h_f – film's thickness

r – radius after deposition

r_0 – radius before deposition

γ^d – dispersive surface free energy

γ^p – polar surface free energy

α – constant phase exponent

Q – flow

H_{pump} – pump's head

P_{pump} – pump's power

P_p – Peak Power

I_p – Peak current

v – solution speed

ρ – density

g – gravity acceleration

p – pressure

h_t – losses

Acronyms/Abbreviations

AFM – Atomic Force Microscope

CA - Contact angles

CVD – Chemical Vapor Deposition

DCMS – Direct Current Magnetron Sputtering

DOMS – Deep Oscillation Magnetron Sputtering

EDS – Energy Dispersive Spectroscopy

EIS – Electrochemical Impedance Spectroscopy

GXRD – Grazing X-Ray Diffractogram

HiPIMS – High Power Impulse Magnetron Sputtering

IMO – International Maritime Organization

MPPMS – Modulated Pulses Power Magnetron Sputtering

OCA – Optical Contact angle

OWRK – Owens-Wendt-Rabel-Kaeble

PP – Potentiodynamic Polarization

PVD – Physical Vapor Deposition

SEM – Spectroscopy Electron Microscope

SFE – Surface Free Energy

SS – Stainless Steel

TBT – Tributyl Tin

WP – Working Pressure

XRD – X-Ray Diffractogram

1. INTRODUCTION

The marine environment has proved to be one of the most aggressive for steel structures in industrial ships, leading to constant immobilization for maintenance, consequently increasing costs. Among various steel structures, the sea chest gratings made of stainless steel are prone to corrosion and biofouling. Biofouling is known as the accumulation of aquatic organisms, these get stuck in the gratings and get dragged into different habitats around the ocean (Castro, 2020). Therefore, protective coatings have been developed for the past decades with the aim to avoid corrosion phenomena and improve the material's properties. However, the most used coatings have been polymeric coatings such as anticorrosive paints, which exhibit toxic products that interfere with the environment stability and biodiversity. In the past years, these concerns grew even more with the necessity to recover the biodiversity in the planet and diminish the impact that industrial ships have in the ocean. This led to the banishment of some of those paints by the International Maritime Organization (IMO), such as the tributyl tin (TBT), which was the most applied paint. Also, polymeric coatings have poor mechanical and anti-degradation properties (Pistone et al., 2021), thus they do not offer that much of a long-lasting protection against corrosive agents and organisms that cause biofouling, which brings out the urge to find multifunctional coatings that could attain these needs and provide good mechanical properties.

Ceramic coatings have been developed with the aim to fulfil these requirements, as they provide good corrosion resistance, good mechanical properties being sustainable for the marine environment, due to the chemical inactivity. The most common ceramic coatings used are some transition metal nitrides or oxide-nitrides such as TiN, ZrN and CrN, although ZrN have proved to be successful at improving the corrosion and wear resistance of stainless steel (Mejía et al., 2022).

These coatings are usually performed in the form of a film deposited by Physical Vapor Deposition (PVD), which represents a main group within deposition techniques, and it is mainly used for thin films with a wide range of applications. Within PVD process, magnetron sputtering is commonly used for enhancing the quality of thin films. This process is characterized by the introduction of particles of an inert gas inside a vacuum chamber,

which are directed from a magnetron to the target, the material to be deposited, and sputtered to the substrate. It has advantages when it comes to energy consumption, substrate cleaning by etching, it creates coatings with good adhesion and good corrosion resistance. It is also able to be performed in a high diversity of materials (Baptista et al., 2018).

Magnetron sputtering has some variants that have been investigated, as the need to improve the density and overall performance of the films increased, such as High-Power Impulse Magnetron Sputtering (HiPIMS). HiPIMS is known by the deposition of denser films, but it also presents lower deposition rates (Baptista et al., 2018). However, for the development of coatings for the naval field, the main necessity is to avoid the corrosive agents to affect the films and deteriorate them. In this sense, dense films are more important than a high deposition rate. Deep Oscillation Magnetron Sputtering is the HiPIMS variant that will be used in this work, and it will be compared against Direct Current Magnetron Sputtering (DCMS) to analyse the main differences and advantages of using the different sources.

The main goal of the present thesis is to develop the initial layer of a multifunctional coating with ZrN, without the anti-biofouling agent, for the application in industrial transport ships that are constantly exposed to seawater. It is important to study deposition parameters in order to control the morphology, structure, roughness, and wettability of the coatings, for achieving good mechanical properties, and high corrosion resistance. By improving the properties of the materials, the lifetime of the ship's structures increases, consequently leading to decrease in the maintenance, increased speed, and less fuel expenses. Contributing, this way, to a more sustainable influence in the ocean, as well as a sustainable economy for transport ships.

2. STATE OF ART

2.1. Coatings for the naval industry

The metals used in ship structures are constantly exposed to the marine environment, which is one of the most aggressive, especially in terms of corrosion. Corrosion is caused by the chemical interaction with this type of environments, which leads to the degradation of the materials and its properties. It can come from many factors, such as chloride ions presence, temperature variations, aerosols, fouling, biofouling, and environmental microorganisms (Laurentiu et al., 2016). Biofouling itself is defined as the accumulation of aquatic organisms, which can be plants, animals, or micro-organism on surfaces that are constantly immersed in sea water. This phenomenon deteriorates the materials and reduces their lifetime, but it's also strongly negative for the ocean, as the organisms attached to the structures are dragged into other habitats, interfering with the marine fauna and flora (Castro, 2020).

Particularly the sea chest gradings (Fig. 1) and filters, the vessels, and other steel-based materials in ship building are one of the highly affected structures from biofouling and corrosion (Castro, 2020).

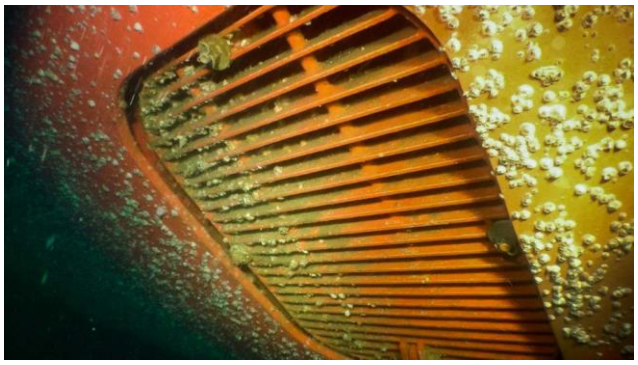

Figure 1. Example of a sea chest exposed to seawater. Extracted from [1].

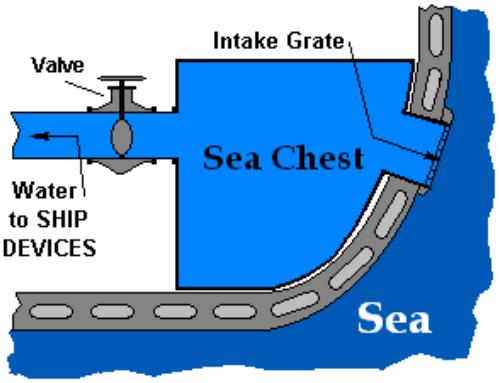

Figure 2. Scheme of a sea chest in a ship. Extracted from [2].

Corrosion problems can lead to an increase of the maintenance costs due to the ship immobilization and possible damage. In the past years, many studies regarding the development of coatings for the steel structures of the ships have been made to avoid

corrosion of these structures and extend their lifetime. Anticorrosive coatings have the role to protect the substrate, providing a barrier against the corrosive agents and hence, improving the materials performance. Steel is the most used material for the naval industry, and although is it a cost-effective material and versatile, it has very low corrosive resistance (Benea et al., 2018). Some coatings used on steel are metallic, ceramic, organic and inorganic (Ulaeto et al., 2017). Organic coatings are usually based on polymers, such as polyurethane, epoxy and polymeric paints (Wood et al., 1998); inorganic coatings are commonly based in inorganic binders, such as silicon resins, water and solvent-based silicates, and silanes (Mu et al., 2017); metallic and ceramic coatings are usually based on Fe, Ni, Cr, Ti, and also nitrides such as CrN and TiN (Wood et al., 1998).

The most common coatings applied through the years in this field were polymeric, more specific the use of polymeric paints, such as the tributyl-tin (TBT), as well as copper and zinc-based systems (Pistone et al., 2021b). However, TBT paint was banned in 2008 by the International Maritime Organization (IMO) because of the impact it has in the marine biodiversity and the environmental threats it presents, since in their composition there are toxic biocides such as mercury, lead, and arsenic (Chambers et al., 2006). These not only affects the ocean but also the human health. As nowadays the concern on maintaining the biodiversity on the planet has become higher, and since biofouling is one of the main problems for the marine environment, the goal has been to find “greener” options for anticorrosive and antibiofouling coatings on steel structures (Pistone et al., 2021a). The aim is to engage a multifunctional performance for the coating, that not only could control the biocide release, being more sustainable, but also resist to corrosion, preventing the ships to be constantly submitted to maintenance. Also, by combining these two mentioned abilities, friction caused by biofouling accumulation would decrease, and thus it increases the speed of the ship, reducing the costs on fuel (Castro, 2020).

Therefore, the main objective with the development of these multifunctional coatings is to guarantee a combination of good mechanical properties, good adhesion to the metallic substrate, and the ability to detach the fouling organism. Also, it is needed a good corrosion resistance, which is the focus of this work.

Some studies on alternative coatings have been made but mostly on polymeric alternatives. Pistone et al. (2021) states that epoxy and silicone-based coatings nowadays represent the main types of coatings used and investigated, but neither of them presents great

adhesion and high hydrophobicity, which is important on avoiding the penetration of the seawater, at the same time. The authors also imply that it is necessary to develop coatings with better mechanical and degradation resistance, being also economically converted into large-scale industrialization.

Other authors studied the use of transition metals nanoparticles, such as TiO2, added to the polymeric coating and noticed some good changes on anticorrosive performance (Benea et al., 2018). The question remaining is why not just develop a coating based on ceramic or transition metals materials, to obtain better corrosion resistance than with polymeric coatings, and being more sustainable for the marine environment.

This work was focused on developing a ceramic nitride coating and it will be simulated its working behaviour for the sea chest gradings of ships, which is the component that filters the seawater supply to ship equipment's (Fig. 2) – like pumps, heat exchangers, counter firing systems, engine cooling and others (Castro, 2020).

The present thesis performed the first part of the multifunctional coating, which would gather good mechanical, anticorrosion and antibiofouling properties, but focusing on the study of the first two features. The coatings developed by this work were made by reactive magnetron sputtering technology, which is environmentally friendly. This layer should be the base for a second layer which would have antimicrobial properties and it will be developed in a future work.

2.2. Physical Vapour Deposition Processes

Physical vapour deposition (PVD) is a well-known technology used for the deposition of thin films concerning several demands, such as tribological behaviour enhancement, visual and optical upgrading, and numerous other fields (Baptista et al., 2018). As it evolved in the past decades, this technique has showed massive improvements, as the aim to improve the coating's characteristics has become more and more important.

The PVD technology can be described as a thermal physical process where the material to be deposited, labelled as target, is transformed into atomic particles that are driven to the substrates in a vacuum environment, and the coating grows on the substrate atom by atom. The PVD reactor consists in two electrodes connected to a high voltage power supply and a vacuum chamber. The fact that the process is in a vacuum environment reduces the gaseous contamination during the process (Baptista et al., 2018).

2.2.1. Magnetron sputtering

Regarding the PVD process, it can be divided in two main methods that depend on how the particles are extracted from the target – sputtering and evaporation (Fig. 3). In the evaporation process, as it generally presents lower atomic energy, it demands for high-vacuum pressure, lesser absorbed gases into the coatings and lower adhesion to the substrate, when compared to the sputtering process, although it shows higher deposition rates. This process is usually used for thicker films and coatings that require lower surface morphology quality. On the other hand, the sputtering method is relevant in many applications where the deposition rate is not the most important characteristic needed for the films, but it is significant to present a great morphological quality, low roughness, fine grains size, controlled stoichiometry, and great mechanical properties (Baptista et al., 2018). Sputtering processing has a significant impact in many areas which need specific properties such as hardness, wear-resistant, low friction, corrosion-resistance, decorative, optical, or electrical (Kelly & Arnell, 2000).

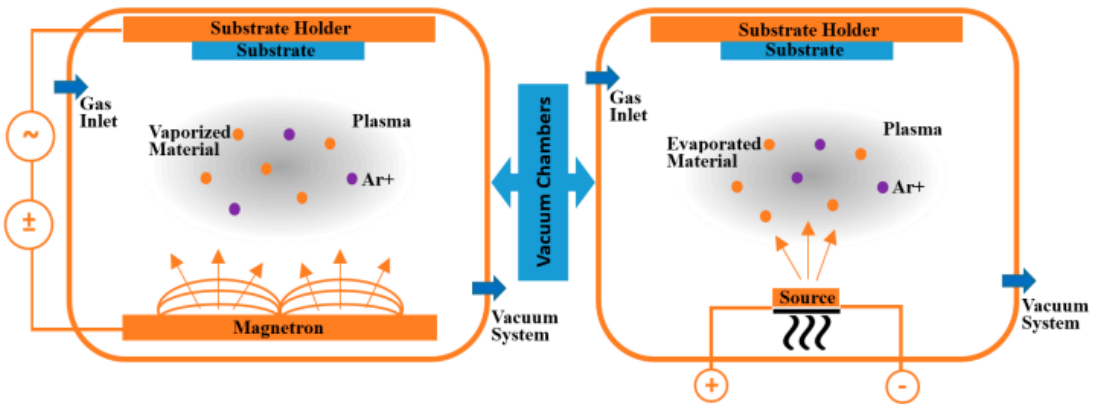

Figure 3. Schematic drawing of two PVD processes: a) sputtering; b) evaporation. Extracted from (Baptista et al., 2018).

In the sputtering process, a high vacuum must be guaranteed to introduce an inert gas, usually Argon, which is ionized in the target vicinity and accelerated by a high voltage creating a potential difference between the target and the substrate. The inert gas particles impact to the target directed by the magnetron, releasing metal particles and electrons. The magnetron consists in a magnetic field near the target that maintains the accelerated electrons

above the target (Strijckmans et al., 2018). The sputtered particles from the target are projected due to the energy transmitted by gas ions to the target particles and driven to the substrate, creating a solid thin film (Baptista et al., 2018).

This entire process of deposition by magnetron sputtering consists of four steps, as describes Baptista et al. (2018) (Fig. 4). The first step, the ramp up stage, entails the setting up the vacuum chamber and activation of the two vacuum pumps - a mechanical pump that induces the primary vacuum (10^3 to 10^{-2} Pa) and a turbomolecular pump for the high vacuum (10^{-2} to 10^{-6} Pa) - to decrease the pressure inside the chamber. The second step is defined as etching or cathodic cleaning, where the bombardment of Ar ions attains to remove surface contaminations and helps increase adhesion and surface quality. Afterwards, the coating process itself takes place in the third step. Commonly, metals are used as targets, but it is possible to use ceramics or polymers to create coatings. Besides, it is possible to use reactive gases to obtain nitrides, oxides, oxynitrides, carbides, among others. Lastly, the ramp downstage initiates and the vacuum chamber returns to room temperature and ambient pressure, by a cooling system. This last stage, the cooling process, can decrease production rate and rise energetic costs, being a disadvantage for industrial applications.

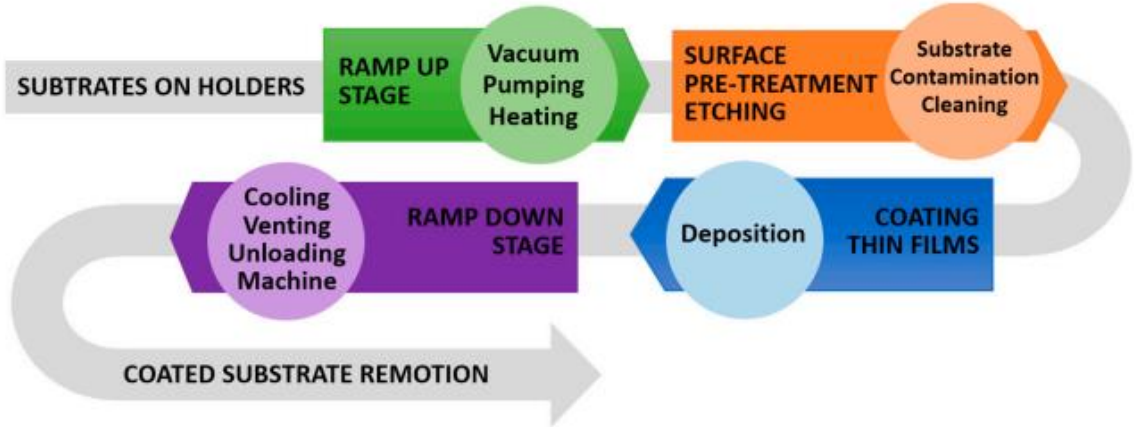

Figure 4. The processing flow of a sputtering process. Extracted from (Baptista et al., 2018).

Magnetron sputtering presents some advantages when compared to other deposition techniques, including substrate cleaning, as it was mentioned earlier, enables better film densification, and reduces residual stresses. It also shows a lower energy consumption when compared to other deposition techniques, such as the Chemical vapor deposition (CVD). Besides, this technology is environmentally friendly and involves low maintenance, which

leads to lower costs and represents an advantage in terms of market demand. This technique is also able to produce coatings with great adhesion, homogeneous layers and high diversity of materials and properties, plus it also improves wear and corrosion resistance (Baptista et al., 2018).

2.3. High Power Impulse Magnetron Sputtering (HiPIMS)

In the past decades, the demand to improve the performance and density of the films deposited by PVD has become higher. For the past fifteen years a new sputtering deposition technique has been developed: HiPIMS (High Power Impulse Magnetron Sputtering), which is becoming closer to the appliance on industrial applications (Ferreira, 2017). Some authors focused on researching the evolution of different techniques and reactors and how they affected the coating properties. During the coating deposition, parameters such as the number of targets, the substrate geometry, the distance between samples and target, the reactor occupancy rate, the gas flow, and others, can be adjusted. Changing some of these parameters can have an impact in the film deposition rate and adhesion, and consequently in the properties (Baptista et al., 2018). Li et al. (2018) studied the effect of the N-Ar ratio on the microstructural and mechanical properties of AlSiN coatings using HiPIMS and the results showed an increase of hardness and better tribological behaviour on the films as the N-Ar flow ratio increased and the nitrogen was up to 56,3%.

In the magnetron sputtering technique, it can be used a DC power source (Direct Current Magnetron Sputtering – DCMS), where the plasma density can be improved by increasing the power applied to the target, but it is limited by the melting point of the target and cooling efficiency by the cathode. Using HiPIMS, the deposition chamber is the same as used with DCMS, except for the power supply equipment, which is applied by short pulses. Therefore, the time average power is similar to DCMS, but the peak power is 100 times higher (Ferreira, 2017). Although it is very versatile and has shown improvements in the coating properties, it is hard to obtain repeatable results with HiPIMS, as it can be quite instable, so it requires some care in the process.

The goal with using this technology is to obtain films with higher density, but it has the disadvantage of a lower deposition rate when compared to DCMS. This is caused by two main factors: the first one is when the ionization of a sputtered atom occurs too close to the target and the energy of that ion is not enough to overcome the potential barrier, the ion will

be back-attracted to the target surface and it results in the return effect that leads to decrease of the deposition rate, instead of contributing to the film growth; the other cause is the high voltages required to operate a HiPIMS discharge when compared to DCMS discharge, which leads to a loss of efficiency of the sputtering process and lower deposition rates (Ferreira, 2017).

2.3.1. Deep Oscillations Magnetron Sputtering (DOMS)

Due to the low deposition rates of the HiPIMS technology, some variants have been researched, such as Modulated Pulses Power Magnetron Sputtering (MPPMS), that has the advantage that it can operate in larger ranges of power density (Ferreira, 2017). However, both HiPIMS and MPPMS techniques hold the disadvantage that some arcs can be created during the process, when operating in reactive mode, originated by the abrupt voltage variations, which can damage the films or force the process to stop by the instability and impossibility to have reproducible results.

In that matter, it has been investigated the use of another variant, Deep Oscillation Magnetron Sputtering (DOMS), which is still in a trial phase of its potentialities. In DOMS, the voltage pulses are constituted by a set of oscillations where the voltage and current increase progressively during the on-time (t_{on}) until they reach the maximum value of Vp – peak voltage – and Ip – peak current, and then they decrease until reaching zero before the end of the period T ($T = t_{on} + t_{off}$). The source is powered by an internal direct current (DCint) power supply and while varying the pulse duration and its frequency. This method allows to achieve higher peak powers and average powers. The power supply software adjusts the pulse frequency to keep the average power, while the peak power could be calculated by Pp = Vp x Ip. There are some parameters that must be defined for establishing the exact pulse to be used, which are the DCint, the duration pulse (D) and the times when the oscillations are on and off (ton and toff respectively). In both DOMS and MPPMS, as it allows for a high degree of ionization, it facilitates the deposition of dense and compact films while avoiding the need for the bombardment of high-energy particles (Ferreira, 2017).

Ferreira (2017) in his Doctoral Thesis analysed this process in detail, comparing the coatings made by DCMS and DOMS using Cr, Ta, CrN and TiSiN. The films deposited by DOMS and with the lowest peak power showed a columnar growth and when increasing the peak power, it is obtained more dense and compact films.

During this investigation, it will also be analysed the differences between films deposited by DCMS and DOMS, with the aim to compare their properties and to evaluate if the use of HiPIMS is justifiable for the ZrN coatings and what possible advantages and disadvantages are seen in the functional properties of the films.

2.4. Zirconium based coatings

Stainless steel (SS) is one of the most used materials in ship structures, but it is proved to be vulnerable to deterioration when exposed to aggressive environments, as already mentioned in the previous section. Surface ceramic coatings used as passive barriers can deliver enduring physical protection against the penetration of water, oxygen, and several aggressive ions (Y. Zhang et al., 2022). Thus, many studies regarding the metal-nitride single layers coatings such as TiN (Elmkhah et al., 2018) and CrN (Ferreira et al., 2016) have been made. One of the disadvantages of these coatings is the columnar microstructure, that results in intrinsic defects such as micropores and cracks, which allow for the corrosive agents to penetrate through the defects and diffuse into the coating layer, reaching the steel substrate (Zhang et al., 2022). Consequently, the development of nitride ceramic coatings produced by HiPIMS have been studied to improve their behaviour and avoid for the corrosive agents to reach the substrate by densification of the films. The most common are TiN, CrN and ZrN, being the last one recently more investigated, while having a similar behaviour to TiN, it has shown to improve the wear and corrosion resistance of stainless steel (Mejía et al., 2022).

Zirconium nitride is a though ceramic which is becoming more attractive in the industry due to its life cost, which has been more competitive, but mostly for the physical properties such as the corrosion resistance, fatigue resistance and high strength (Ferrando, 1988). Also, zirconium nitride coatings produced by PVD are being highly used in the industry because of the various mechanical and tribological applications (J V Menghani 1 et al., 2018). Besides, as it is a chemically inactive material, it does not present a threat to the marine environment.

Milosev et al. (1997) compared the behaviour of ZrN, TiN and CrN coatings by electrochemical and thermal oxidation. According to the obtained results, TiN and ZrN exhibited similar behaviours. The main differences were on the air oxidation impact, which induces minor changes in CrN when compared to ZrN and TiN. However, both ZrN and TiN

can build up a passivation layer which offers them an oxidation and corrosion resistance (Pejaković et al., 2015). In another study, regarding the corrosion behaviour of ZrN coatings, the ZrN coated sample showed much lower corrosion rate than uncoated stainless steel when exposed to 3,5% (w/w) NaCl solution, although the defects formed in the coating are impossible to avoid corrosion completely (J V Menghani 1 et al., 2018).

Zirconium nitride is also characterized by its high hardness, good chemical stability, and biocompatibility. Commonly, the nitrogen is introduced with the aim to improve the tribological properties of the films constituted by zirconium and, as the level of nitrogen is increased, some changes occur in the surface features, such as roughness and the crystalline size of the coatings (Kuznetsova et al., 2020). Purandare et al. (2011) performed the deposition of ZrN coatings by HiPIMS which resulted in dense coatings with good adhesion and hardness.

In this work, the optimization of the ZrN layer will be performed by controlling some parameters – the partial pressure of Argon and the reactive gas (Nitrogen), time, and power in the Zr target. Primarily, a stoichiometric ZrN film will be developed by DCMS and used as reference in the characterizations of the ZrN systems obtained by HiPIMS.

3. EXPERIMENTAL METHODOLOGY

3.1. Introduction

The aim of the present work is to develop and optimize the deposition of a ZrN coating to avoid corrosion and improve the mechanical properties of steel used in sea chest gratings. The experimental methodology is explained in detail in this chapter.

The first stage was to prepare all the substrates for the depositions and characterizations of the coatings. As aforementioned, 316 L stainless steel (SS) was used for its common use in the sea chests gratings. Also, silicon (Si) wafers were coated to study some of the film's properties. Hence, 20x20 mm^2 SS coupons were polished using wet sandpapers of different grits (320,600,800, and 1200 grit consequently) to take off most of the scratches from the surface. Besides, it was used a polishing machine with 6 and 3 µm diamond paste to obtain a mirror appearance finishing. Similarly, the Si wafers were cut in 18 x 18 mm^2 to fit to the substrate holder. All the polished uncoated substrates were cleaned with acetone and ethanol by ten minutes each in an ultrasonic bath.

The films were characterized by several techniques. The physical, chemical, and structural properties were disclosed by Scanning Electron Microscope (SEM) (morphology), Energy Dispersive Spectroscopy (EDS) (chemical composition), X-Ray Diffraction (XRD) (structure), Atomic Force Microscopy (AFM) (topography) and Optical Contact Angle (OCA) measurements (wettability and surface energy). Then, the mechanical characterization was unveiled using nanoindentation measurements (hardness), residual stress, and scratch test according to the STM C1624-05 standard (film adhesion strength). Lastly, the coatings were functionally characterized, through Electrochemical Impedance Spectroscopy (EIS) and Polarization Potentiodynamic (PP) tests to assess its corrosion resistance. The parameters and methods used for all these experiments will be detailed later.

3.2. Deposition of ZrN films

The films were performed at CEMPPRE in the Mechanical Engineering Department, using a vacuum chamber made of high-grade stainless steel (Fig. 5). This chamber can be connected to different kind of power source (Fig. 6). To achieve high vacuum base pressure

(~10^{-4} Pa), the chamber counts with two vacuum pumps (mechanical pump and turbomolecular pump). Besides, it contains a rotation system with adjustable velocity for the substrate holder, a shutter which acts as a barrier between the target and the substrate, and a software to control the power source parameters. The target used in this work was Zr (99% purity – Testbourne) with 150x150 mm^2 surface and 8 mm thickness. Two different power sources were used to obtain the studied films. The DOMS power source was a Cyprium III plasma generator (Zpulser Inc.) and the DCMS power source was a Huttinger PFG 7500 DC.

Figure 6. High-Impulse power source.

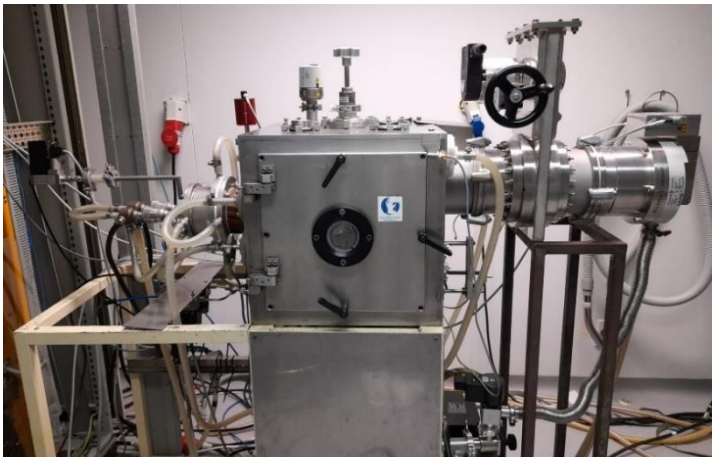

Figure 5. Deposition chamber used in this work.

Before any deposition, tests were made in the chamber to adjust the sputtering process to achieve sputtering reactive mode, and always using Argon as working gas. In this prelimary study, a constant power (1200 W) was applied to the target, and nitrogen was injected progressively (0 ~100 % N_2 flow). The hysterisis curve (Fig. 7) shows a first zone labelled as metallic mode, whereas the zirconium in the target is expelled from the target but it poorly reacts with the low nitrogen flow inside the chamber. Later, it starts the transition mode, represented by an abrupt rise of potential. According to (Carvalho, 2008) this potential increasing could be related with the formation of ZrN on the target surface. This rise in the target potential is also due to the secondary electron emission yield (Rebelo et al., 2016). In the last stage, the target potential stabilizes no matter the nitrogen incrase. At this point, the target is "poisoned" and stoichoimetric ZrN is being formed. This operation point is commonly known as the reactive mode. Since the goal is to perform zirconium nitride, it is

necessary to work in the reactive mode. Therefore, six different tests were made to achieve the reactive mode for DOMS, varying different charging voltage (DCint) of the power supply - 250V, 300V and 350 V at 0.4 Pa working pressure and 250V at 0.7 Pa working pressure. For DCMS there were performed two hysterisis curves at 0.4 Pa and 0.7 Pa working pressure. The average power in both processess (DCMS and DOMS) was constant during all the tests and later depositions (1.2kW).

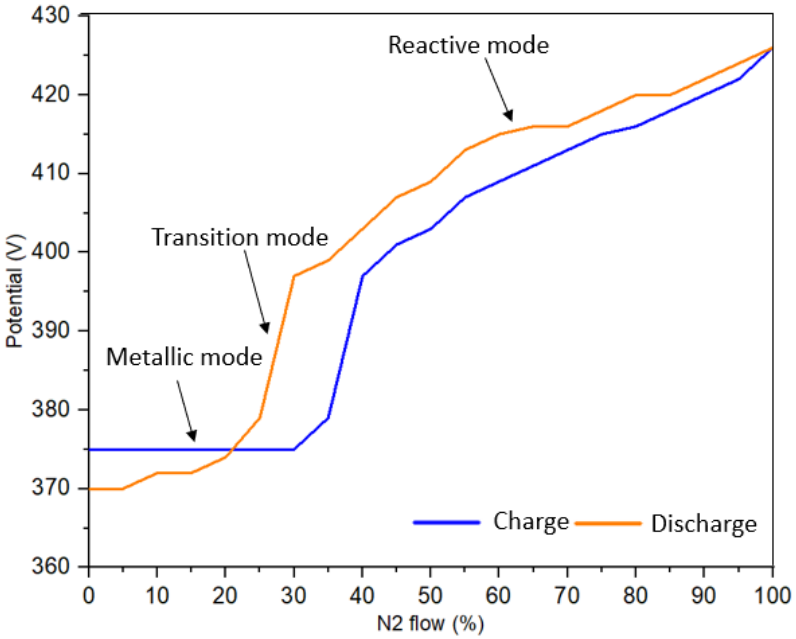

Figure 7. Hysterisis performed with DCMS at 0.4 Pa working pressure.

At first there were selected ten different films to deposit, but in some of them the source started to fail, which can happen during HiPIMS depositions, and to obtain acceptable results only seven films were deposited - two films by DCMS and five films by DOMS, with different nitrogen flows, charging voltage and two different working pressures (0.4 Pa and 0.7 Pa).

Prior to any deposition, there were made some tests using only silicon samples inside the chamber, to measure the thickness and then, calculate the deposition time. In every film, firstly an interlayer of pure zirconium was deposited, aiming to improve the film's adhesion. The deposition time was determined with the aim to reach 300 nm of the Zr interlayer and 1µm of total thickness. The values of thickness obtained and the deposition times for each coating are shown in Table 1 and 2. The coatings are labelled according to the deposition parameters (ZrN-Working Pressure-DC_{int}-N_2 flow).

Table 1 - ZrN films obtained at 0.4 Pa working pressure after initial tests.

	N_2 flow (%)	Thickness (nm)	Deposition time (s) Zr layer / ZrN layer
ZrN-0.4-45	45	670	298 / 2687
ZrN-0.4-300-30	30	365	400 / 4932
ZrN-0.4-300-40	40	322	400 / 5590
ZrN-0.4-300-80	80	195	400 / 9231
ZrN-0.4-350-80	80	177	475 / 8723

Table 2 - ZrN films obtained at 0.7 Pa working pressure after initial tests.

	N_2 flow (%)	Thickness (nm)	Deposition time (s) Zr layer / ZrN layer
ZrN-0.7-50	50	644	225 / 2795
ZrN-0.7-250-50	50	418	356 / 4337

For the deposition of the films, it is necessary, as already mentioned, to clean the target and substrate. This process was done during one hour before each deposition, applying 350 V pulsed voltage (120 KHz pulse frequency – 1616 ns pulse width) to the substrate and 250 W power (DC) to the target. Also, the shutter was positioned between the substrates and the target. After the cleaning process, the deposition began using 1.2 kW of average power, performing a first thin layer of zirconium and a second layer of zirconium nitride. The rotation speed was kept at 23,5 rpm. The t_{on}, T and D were 12s, 36s and 1000s, respectively. The parameter's values given by the software of the DOMS depositions are presented in the Table 3 and from the DCMS depositions in Table 4.

Table 3 - Parameters of ZrN films obtained by DOMS.

	N_2 flow (%)	Charging voltage - DCint (V)	Working Pressure – WP (Pa)	Peak Voltage - Vp (V)	Peak Current - Ip(A)	Peak Power – Pp (kW)	Frequency (Hz)
ZrN-0.4-300-30	30	300	0.4	-1066	126	134	131
ZrN-0.4-300-40	40	300	0.4	-1063	109	116	132
ZrN-0.4-300-80	80	300	0.4	-1054	93	98	138
ZrN-0.4-350-80	80	350	0.4	-1232	152	187	78
ZrN-0.7-250-50	50	250	0.7	-867	64	56	194

Table 4 - Parameter of ZrN films obtained by DCMS.

	N_2 flow (%)	Working Pressure - WP (Pa)	Voltage -V (V)	Current – I (A)	Power – P (W)	Bias Voltage (V)	Bias Current (A)
ZrN-0.4-45	45	0.4	-365	3	1230	-50	1.2
ZrN-0.7-50	50	0.7	-358	3	1231	-50	1.4

For the DOMS deposition, an oscilloscope is attached to the system, which indicates the pulses of P_p and I_p (red pulses for voltage and yellow pulses for current), connecting to the software that shows the frequency values and pulse width. Figure 8 shows an example of the images obtained by this oscilloscope.

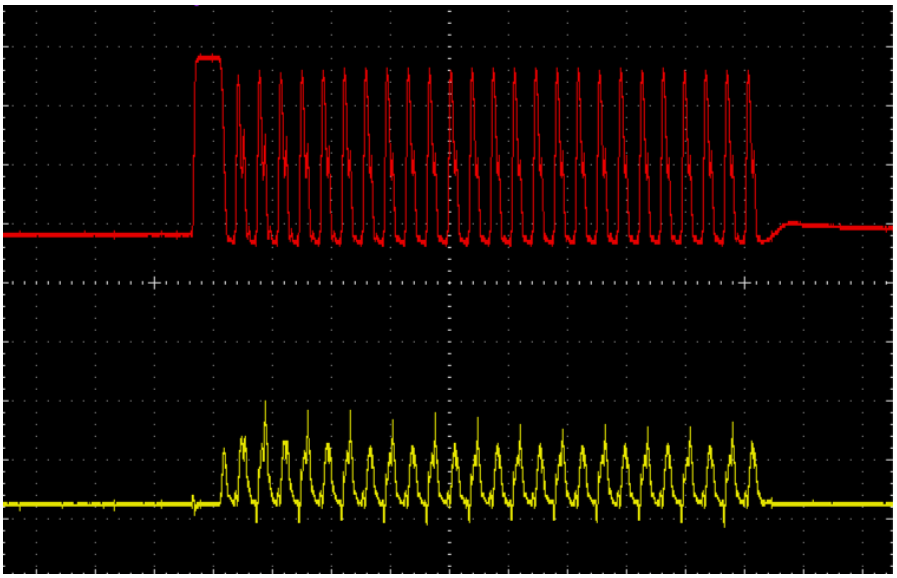

Figure 8. Example of deep oscillation pulses during the deposition by DOMS. Image obtained from the oscilloscope.

3.3. Physical, chemical, and structural characterization

3.3.1. SEM and EDS

The analysis of the morphology of each coating was performed by Scanning Electron Microscope (Hitachi SU3800). This equipment allows for a higher magnification range than a normal optical microscope and it consists in the incidence of an electron beam in the sample

surface. Along with this, Energy Dispersive Spectroscopy (EDS), equipped with the SEM, was used to analyse the chemical composition.

The value of accelerated voltage of the particles (Vacc) was 10 kV for the secondary electron images, 15 kV for the EDS analysis, and working distance was 10 nm.

3.3.2. XRD

For the characterization of the coatings structure, Grazing Incidence X-Ray Diffraction (GIXRD) was performed. This allows for the determination of the crystalline phases and the structural properties such as the grain size, the orientation, and structure defects (Caratão, 2014).

It was used the PANalytical X'Pert PRO MPD with CuKα radiation (45kV and 40mA) and $\theta = 3^{\circ}$. Using a pseudo-Voigt function, the XRD spectra peaks were fitted to calculate the area and position of the peaks (2θ). The lattice parameter was determined by the Bragg's law, using the geometrical relationship between the lattice parameter, the interplanar distance and Miller indices (Ferreira et al., 2016).

3.3.3. AFM

In order to characterize the surface topography, Atomic Force Microscopy (AFM) was carried out with Bruker Innova equipment with a Si tip of nominal 6nm radius used in tapping mode. With this test, the roughness and porosity of the films can be analysed. Several scans of 3x3 μm^2 area were acquired to guarantee a good surface representation. For the post processing of the AFM images, it was used the Gwyddion software. (Ferreira et al., 2016). This software enables the values of roughness, skewness and kurtosis.

3.3.4. Wettability

This characterization is brought out to perceive how the liquids interact on the surface. The wettability tests were made using optical contact angle (OCA) measurements, which examines the contact angle between a liquid and a solid surface, which is caused by the intermolecular force created in their interface (Caratão, 2014).

The equipment used was Dataphysics OCA20. Ultrapure water (99,9%), glycerol and α-bromonaphthalene were used for calculations of the surface free energy according to the Owens-Wendt-Rabel-Kaeble (OWRK) method, which is a standard method for calculating

the surface free energy of a solid from the contact angle with several liquids. 3,5% (w/w) NaCl solution (labelled as Brine) was used to study the wettability in a "real" scenario and correlate it to the corrosion results (Castro et al., 2022).

3.4. Mechanical characterization

3.4.1. Scratch test

The scratch test, as the name indicates, is the act of scratching the sample while applying a load by a diamond stylus, with the aim to analyse the adhesion strength, the failure modes, and the mechanical integrity of a hard ceramic coating (*ASTM C1624-05*, 2010).

These tests were made by the application of a progressive load, scratching three times each sample. While analysing the scratches in the microscope, it can be seen three critical stages: the first critical load is when the coating shows an initial failure, the second critical load is in which the coating starts to detach from the substrate and the third critical load is when the coating detaches 50% from the substrate (Carvalho, 2004). The progressive load applied in these measurements was 70 N and the samples were always pre-loaded applying 3N.

3.4.2. Residual stresses

The residual stresses were obtained by measuring the deflection of the films over Si substrates and using the methodology proposed by (Shiri et al., 2016). It was carried out an average of the stresses, being representative for the entire sample. The measurements were made with a contact profilometer equipped with a diamond stylus. The value of residual stress is calculated by the Stoney's equation (Shiri et al., 2016):

$$\sigma_f = \frac{E_s}{1-\nu_s}\frac{{h^2}_s}{6th_f}\left(\frac{1}{r}-\frac{1}{r_0}\right) \quad (1)$$

Where σ_f is the residual stress, E_s the young's modulus, h_f and h_s represent the film and substrate thickness, respectively, and r_0 and r the radius before and after deposition (Shiri et al., 2016). The values of r and r_0 are determined according to the technique

developed by (Ramsey et al., 1990) where the substrate curvature is simulated with a second-degree polynomial:

$$f(x) = a + bx + cx^2 \quad (2)$$

The deflection radius is calculated by equation (3).

$$r = \frac{1}{2C} \quad (3)$$

After representing the baseline deflection curve, it is determined the stresses for each direction x and y, σ_x and σ_y, using the equation (1), and then it is calculated the surface average.

3.4.3. Nanoindentation

With the aim to evaluate the hardness and the Young's modulus of the coatings, nanoindentation tests (Micro Materials NanoTest) were carried out. A Berkovich diamond pyramid indenter was used. The hardness was evaluated by load-displacement curves with the depth-sensing method, with the load of 5 mN to ensure an indentation depth less than 10% of the coating's thickness and hence, avoiding the substrate interference in the hardness assessment. The loading time, maximum load time and discharge time were all 30 s.

3.5. Functional characterization

After characterizing the coatings fundamentally, with the above-mentioned technologies, the results must be correlated with the functional performance of the films. For this investigation the main objective is to optimize an anti-corrosive coating, therefore, corrosion tests must be performed on every coated sample. Uncoated polished stainless steel was used as control.

The parameters and applied configuration for all these experiments are described in this section.

3.5.1. Corrosion tests

The corrosion tests were carried out by two tests – Electrochemical Impedance Spectroscopy (EIS) and Potentiodynamic polarization (PP). Both corrosion tests were performed at CEMPPRE using a Faraday cage to isolate the samples from electromagnetic external interferences from the outside. The electrolyte used in all the experiment was artificial sea water (3.5% (w/w) NaCl solution in deionised water). The artificial sea water was deposited in the electrochemical cells (Fig.9).

The experiments were made using a three-electrode configuration, with a reference electrode (saturated calomel electrode with KCl), a counter electrode (Pt) inserted in the cell and the studied sample as the working electrode. All the measurements were performed in a Gamry 600 potentiostat. Before any measurement, the cell potential was stabilized (represented by the open circuit potential (OCP)) for one hour.

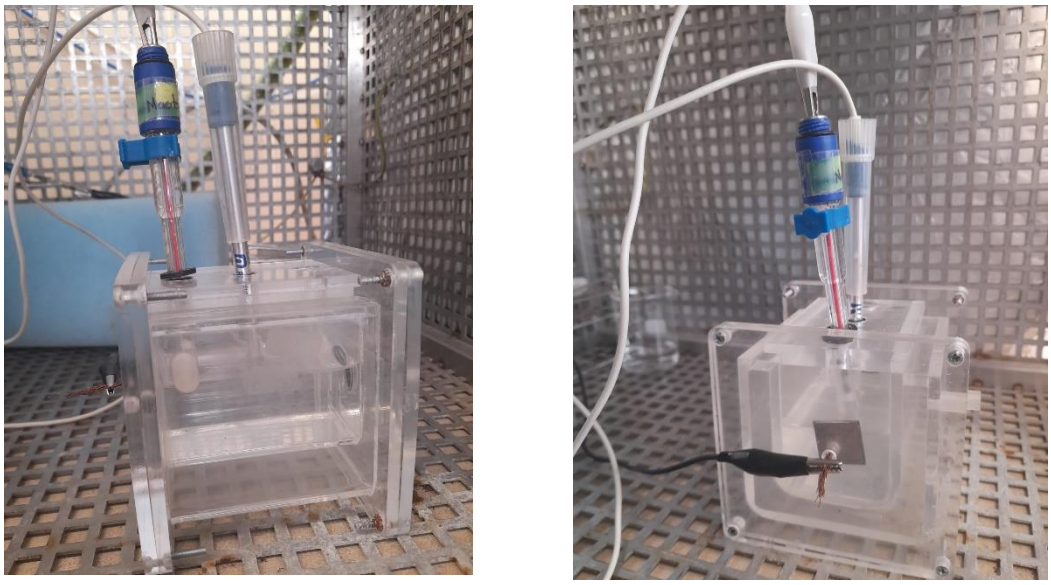

Figure 9. Representation of the set-up used for the corrosion tests inside the Faraday cage.

EIS measurements were made at 0h, 24h, 48h, 72h, 96h and 168h of artificial seawater exposure. EIS measures were performed getting 10 points/decade, using 10 mV rms, between 100 kHz and 0.01 Hz frequency.

For the potentiodynamic polarization experiment, -500 mV and 500mV vs. E_{ocp} was applied with 1mV/s scan rate in three different points of the sample surface. The GAMRY Echem software was used to fit all the corrosion spectra obtained from the two experiments

(EIS and PP). Corrosion rates were calculated using the equivalent weight obtained from the EDS measurements, and applying the procedure proposed by the ASTM G102-89 standard (*ASTM G102-89*, 1999).

4. RESULTS AND DISCUSSION

This chapter exhibits in detail all the results that support the study of ZrN coatings and the assessment of the coatings to be applied in sea chest gratings. Chemical, physical, structural, and mechanical properties are analysed and later, correlated to the functional performance of the coatings. The results were compared to the uncoated stainless steel and supported by other author's studies, evaluating the advantages or disadvantages in the use of HiPIMS. Results are commonly separated by films deposited at 0.4Pa and 0.7Pa, in which the stoichiometric DCMS coating is always presented first as the control. The coatings are labelled according to the deposition parameters (ZrN-WP-DC_{int}-N%).

4.1. Chemical, physical, and structural results

4.1.1. Morphology and chemical composition

The results from the SEM analysis allow the evaluation of the surface morphology, thickness, and hence, deposition rate of the ZrN coatings, and to compare these properties of films deposited by DCMS and DOMS. The values of thickness, deposition rate and chemical composition are displayed in Table 5 and 6. The control film is the DCMS deposited at 0.4Pa with 45% of nitrogen flow (ZrN-0.4-45).

From the thickness and deposition time for each coating (Table 1 and 2), the deposition rates were calculated. It is possible to notice that the deposition rate of films deposited by DCMS is higher than the deposition rate by DOMS coatings. The low deposition rate in HiPIMS coatings was expected, since it is well documented in literature that this technology has a lower sputtering efficiency, which can be due to the return effect or the yield effect (Ferreira et al., 2014). Anders (2017) also explains that when the target gets more poisoned, the sputter yield decreases which leads to a further reduced deposition rate. As the rate decreases, it is also seen a slight decrease in peak power (Table 7). Nonetheless, every DOMS coating exhibits high peak powers in the order of 100 kW, except for ZrN-0.7-250-50 that decreases around 50% compared to the others.

By EDS characterization it is possible to analyse the chemical composition of the coatings. DCMS films have basically a stoichiometric composition. In DOMS, with the

addition of nitrogen, it is noted the decrease of zirconium and increase of nitrogen, although still close to stoichiometric. This phenomenon can be caused by the low deposition rate which decreases the number of atoms in the chamber, leading to less zirconium. Regarding the thickness of the coatings, the goal was to attain 1µm of total thickness (for comparing functional properties purposes), which was accomplished in most of the coatings, being the thinner film the one with the lowest internal voltage in DOMS deposited at 0.7Pa of working pressure (ZrN-0.7-250-50).

As the nitrogen increases, the P_p decreased (see Table 7), which disagrees with several authors who describe an increase in P_p as the deposition becomes more reactive, hence with more nitrogen (Oliveira et al., 2015) (Tang et al., 2020). However, the P_p decrease is not so intense since every coating with DC_{int} of 300V keep around 100kW. With the increase of DC_{int} to 350 V (ZrN-0.4-350-80), shown a high increase in P_p. Regarding the P_p at 0.7 Pa working pressure (ZrN-0.7-250-50) decreased significantly, which was influenced by the lower DC_{int} voltage and the increase of working pressure.

Table 5 - Chemical composition, thickness and deposition rate of the films performed with 0.4 Pa.

	DCint (V)	N_2 flow (%)	Zr (at %)	N (at %)	Thickness (mm)	Deposition rate (nm/s)
ZrN-0.4-45	-	45	50 ± 1	50 ± 1	966 ± 2	0.36
ZrN-0.4-300-30	300	30	47 ± 1	53 ± 1	1328 ± 2	0.27
ZrN-0.4-300-40	300	40	48 ± 1	52 ± 1	1309 ± 2	0.23
ZrN-0.4-300-80	300	80	44 ± 1	56 ± 1	1164 ± 3	0.13
ZrN-0.4-350-80	350	80	45 ± 1	55 ± 1	1027 ± 3	0.12

Table 6 - Chemical composition, thickness and deposition rate of the films performed with 0.7 Pa.

	DCint (V)	N_2 flow (%)	Zr (at %)	N (at %)	Thickness (nm)	Deposition rate (nm/s)
ZrN-0.7-50	-	50	51 ± 1	49 ± 1	925 ± 2	0.33
ZrN-0.7-250-50	250	50	48 ± 1	52 ± 1	780 ± 3	0.18

Table 7- Peak power of HiPIMS films.

	Peak power, Pp (kW)
ZrN-0.4-300-30	134
ZrN-0.4-300-40	116
ZrN-0.4-300-80	98
ZrN-0.4-350-80	187
ZrN-0.7.250.50	56

The film's morphology is given in top view and cross section in Figures 10, 11 and 12. It is evident that the coatings deposited by DCMS displayed a well-defined columnar profile growth, (Fig. 11a and 12c), typical of zone 1 of the Anders diagram (Fig. 13). On the other hand, the ZrN films deposited by DOMS at 0.4 Pa working pressure, especially those with 300 V of DC_{int} (Fig. 11b to 11e) exhibited a much denser and featureless layer, without visible columnar grains in the surface. This is typical of zone T of the Anders diagram, more specifically in the high energy zone, which represents a dense film with reduction of deposition rate (Table 5). However, the DOMS film deposited at 0.7 Pa working pressure (ZrN-0.7-250-50) (see Figure 12b and 12d) exhibits a columnar profile growth which resembles the DCMS films. This was clearly influenced by the high decrease in the peak power (Table 7) and the lower nitrogen flow (50%).

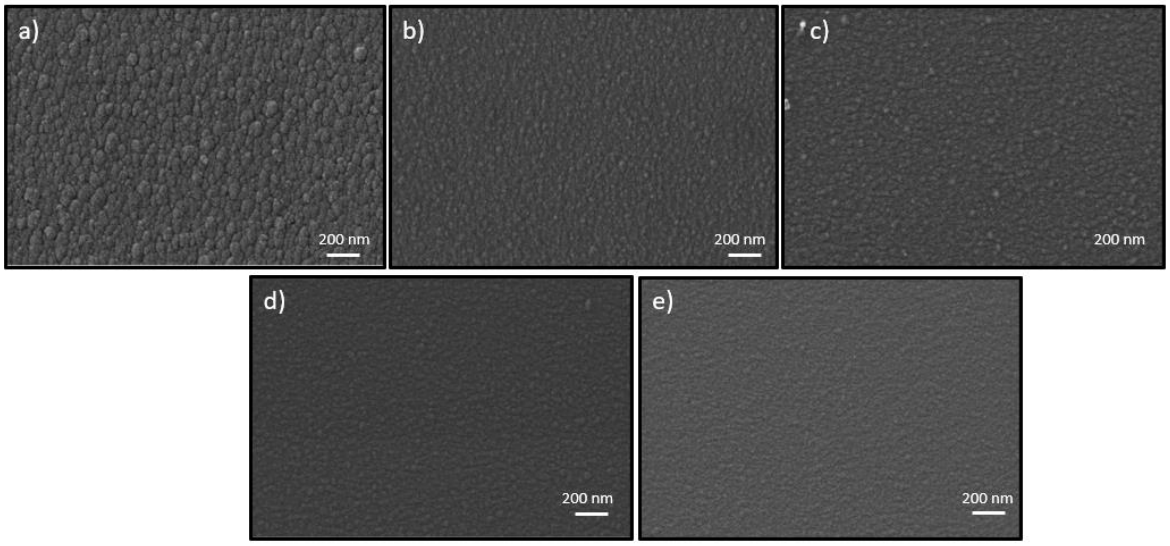

Figure 10. Top view images obtained by SEM of 0.4 Pa films: a) ZrN-0.4-45; b) ZrN-0.4-300-30; c) ZrN-0.4-300-40; d) DOMS-3; e) ZrN-0.4-300-80; f) ZrN-0.4-350-80.

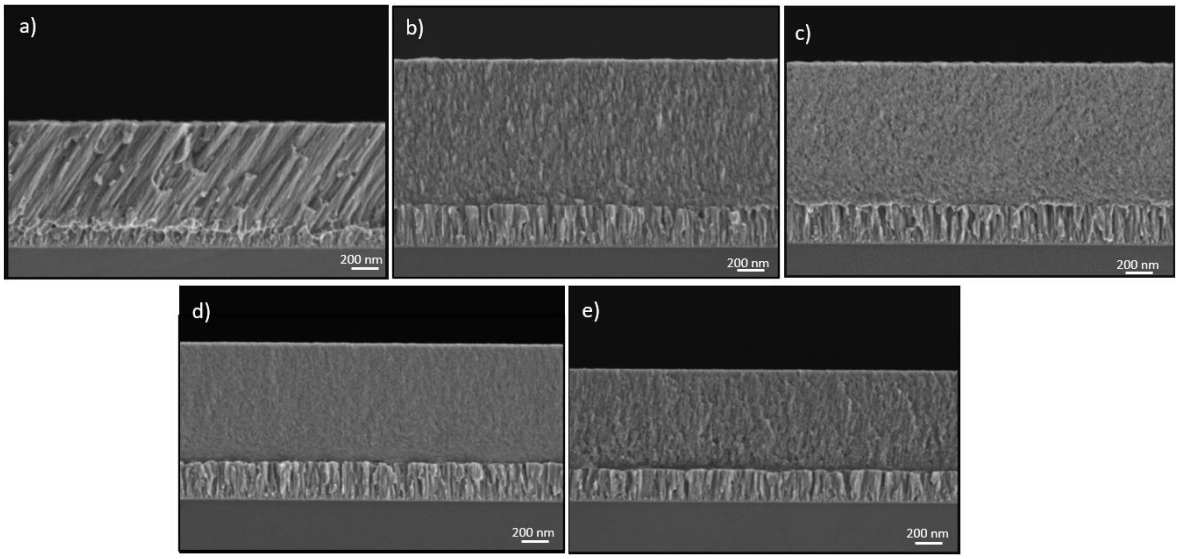

Figure 11. Cross section view images obtained by SEM of 0.4 Pa films: a) ZrN-0.4-45; b) ZrN-0.4-300-30; c) ZrN-0.4-300-40; d) ZrN-0.4-300-80; e) ZrN-0.4-350-80

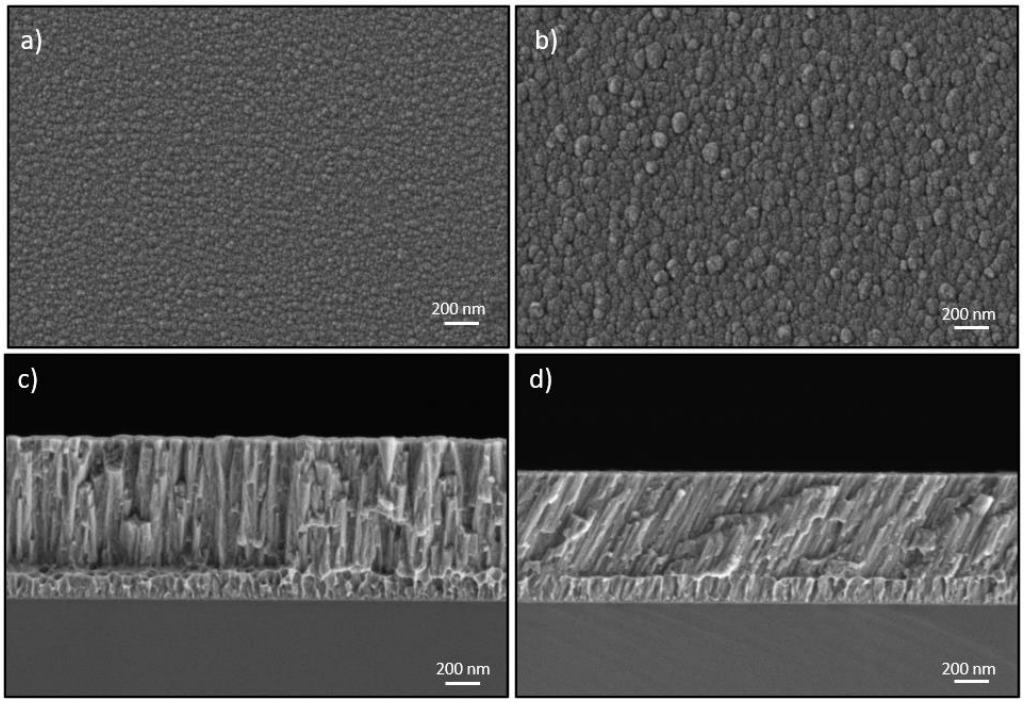

Figure 12. Top view and cross section images obtained by SEM of 0.7 Pa films: a) and c) ZrN-0.7-50; b) and d) ZrN-0.7-250-50.

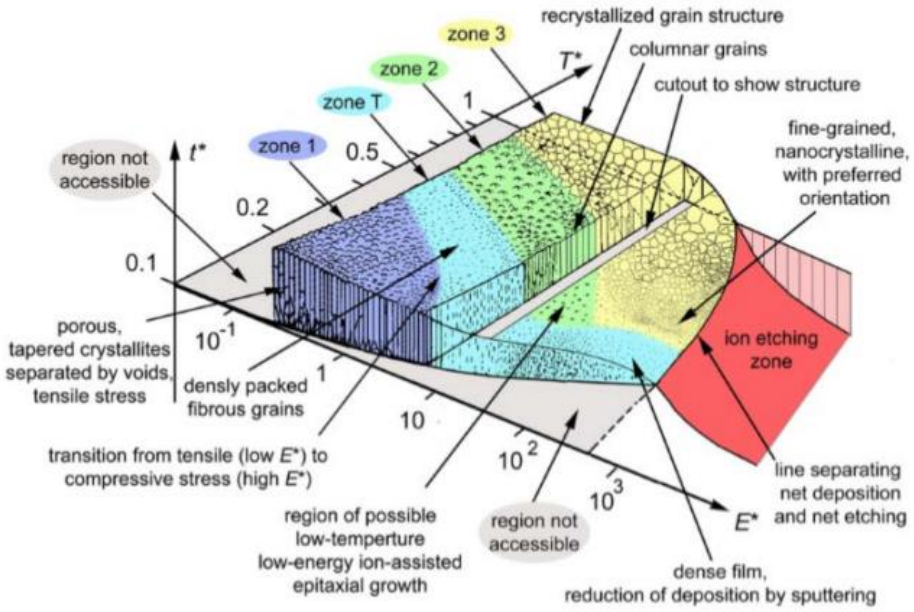

Figure 13. Structure zone diagram applied to HiPIMS films proposed by Anders. Extracted from (Anders, 2010).

4.1.2. Structure

The grazing X-ray diffractograms assess the evolution of the crystallographic structure of the coatings, allowing the identification of the different phases and peaks. The identified crystalline phases are fcc-ZrN (ICDD card no. 035-0753) and hexagonal-Zr (ICDD card no. 005-0665). The ZrN common peaks presented are (111), (200) and (220) in both 0.4Pa and 0.7Pa films. The (200) ZrN plane is only present in the DCMS films and ZrN-0.4-300-30.

The changes in the crystallinity of the films are obvious with the increase of nitrogen. Concerning the films obtained by 0.4 Pa working pressure (Fig. 14), the preferential orientation for the ZrN-0.4-45 film and DOMS with low nitrogen flow is (111), like the described by some authors (Kuznetsova et al., 2020), and as the nitrogen level increases up to 80%, the preferential growth shifts to the (220) plane. This film is extremely crystalline, demonstrating a substantial increase by the intensity of this preferential plane (see Figure 14). This is accompanied with an increase in the grain size to 35 nm, while ZrN-0.4-300-30 and ZrN-0.4-300-40 were just in the range of 5 - 6 nm. The grain size of the ZrN-0.4-45 film

was 4 nm, much smaller than the size of the coatings deposited by DOMS. The shift in preferential orientation can be caused by the change of the ratio ion – atom during deposition, given that more nitrogen is introduced, less zirconium is inside the chamber, as aforementioned, and consequently less atoms. Therefore, with this high ion bombardment, the ion-atom flow increases, and the texture is modified by consequence (Purandare et al., 2014). Also, the intensity of the (220) plane increases as the peak power of the films at 300 V decreases (see Table 7), and when the internal voltage was 350 V (ZrN-0.4-350-80), the peak power strongly increases and the intensity of the peak drops again. ZrN-0.4-350-80 exhibited a different phase of Zr (002) appearing at 35º, whereas in the other films the Zr phases appear at around 36º (101) and 63º (103), associated with the interlayer. This could be related to the substrate's condition, which could present some impurities or scratches, which cause different nucleation.

Figure 15 shows an inset of the (101) Zr plane in the DOMS coatings performed at 300V and 0.4 Pa working pressure, exhibiting the decrease of this phase intensity as the nitrogen flow increases. This indicates that the structural zirconium is decreasing, and the films become more metallic which could influence the mechanical and functional behaviour further on.

Regarding the films obtained at 0.7 Pa working pressure (Fig. 16), the shift of the preferential plane of the ZrN phase was from the (200) plane in ZrN-0.7-50 to the (220) plane in ZrN-0.7-250-50. In this system, the intensity of the preferential peak was smaller than in the above-mentioned system, but it is clear that the implementation of HiPIMS contributed to the film crystallinity increase.

The deviation to the smaller 2θ position of the detected peaks in the films, explained by the existence of compressive stresses, and proved by increase on the lattice parameter, calculated with the Miller indices and the interplanar distance. The lattice parameter of the coatings varied from 4.61 to 4.64 Å, which are higher than the ZrN pattern lattice parameter, which is 4,58 Å ($a_{coating} > a_{pattern}$), and hence exhibiting a distortion of the lattice (Ferreira et al., 2016).

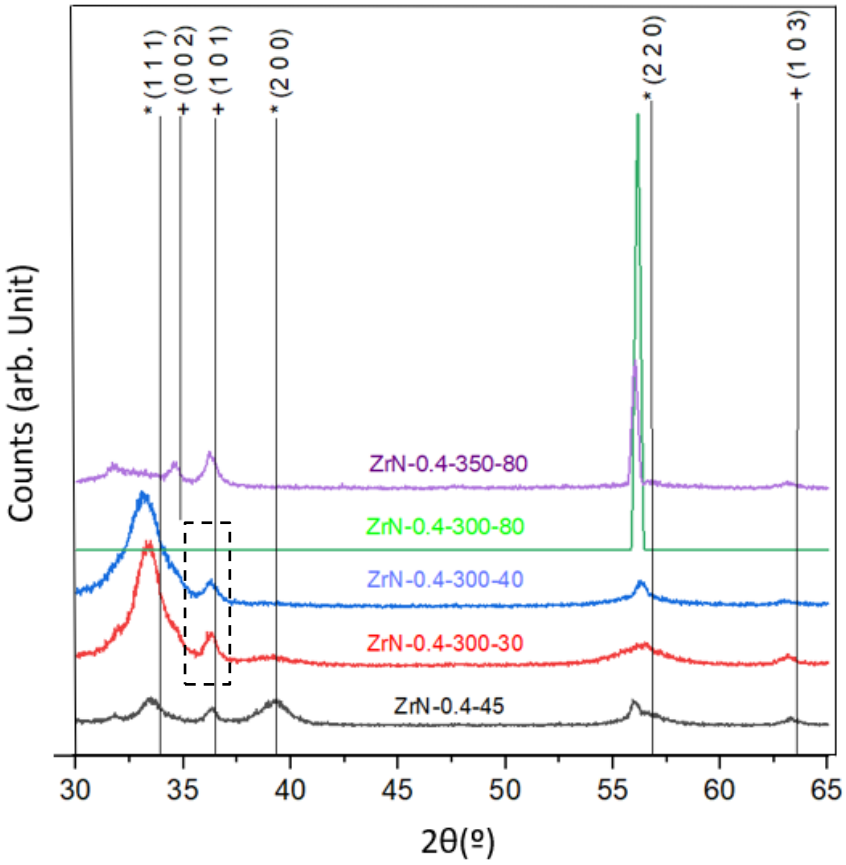

* fcc-ZrN (ICDD card no. 035-0753 + hexagonal-Zr (ICDD card no. 005-0665)

Figure 14. XRD diffractograms of 0.4 Pa films.

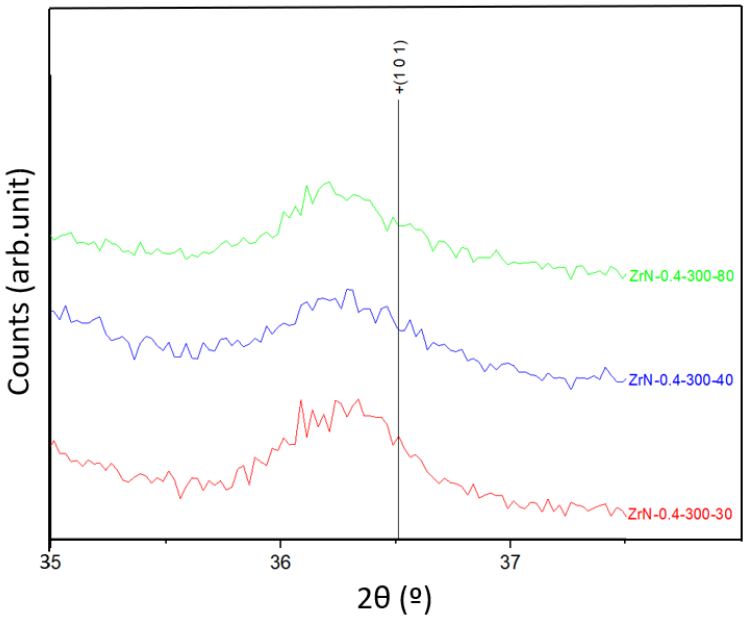

Figure 15. Inset of the dash enclosed area in Figure 14.

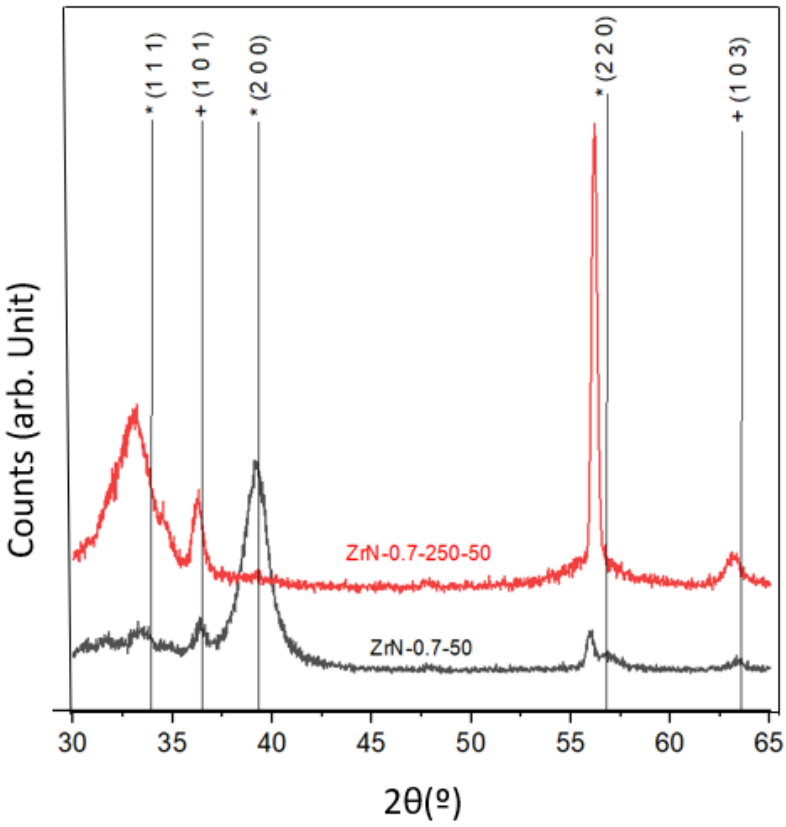

* fcc-ZrN (ICDD card no. 035-0753 + hexagonal-Zr (ICDD card no. 005-0665)

Figure 16. XRD diffractograms of 0.7 Pa films.

4.1.3. Roughness and porosity

The topography of the coatings was assessed by AFM images, where the roughness parameters are obtained over an area of 3x3 μm^2 in each sample. In Figures 17 and 18 there are presented the surface topography and 3D views of films obtained at 0.4 Pa and 0.7 Pa working pressure, respectively. The roughness attends the value of mean roughness, Sa, and root mean square roughness, Sq, whose values are exhibited in Table 8 and 9. The roughness is influenced by the microparticles height, the micro holes depth and the surface topography (Kuznetsova et al., 2020).

All coatings appear to have a very low roughness, except for the ZrN-0.4-300-40 film which exhibits the highest S_a and S_q values (7 and 10 nm, respectively). Both films with 80% nitrogen flow (ZrN-0.4-300-80 and ZrN-0.4-350-80) displayed remarkable smoothness, influenced by the dense morphology obtained according to the SEM images (Fig. 11d and 11e) and the highly oriented structure. Obtain low roughness in films is crucial

to avoid the corrosive agents as seawater, to susceptible substrates (like metals). This feature makes more difficult the penetration of the corrosive agent into the film, which is more likely in dense films. This is proved by the results seen in AFM which showed that the denser coatings exhibited lower roughness, as prove ZrN-0.4-300-80 and ZrN-0.4-350-80. DCMS films display slightly higher values of roughness, around 6 nm, having a columnar growth. However, these results suggest that the roughness did not influence much the other properties, since these values cannot be considered as rough surfaces.

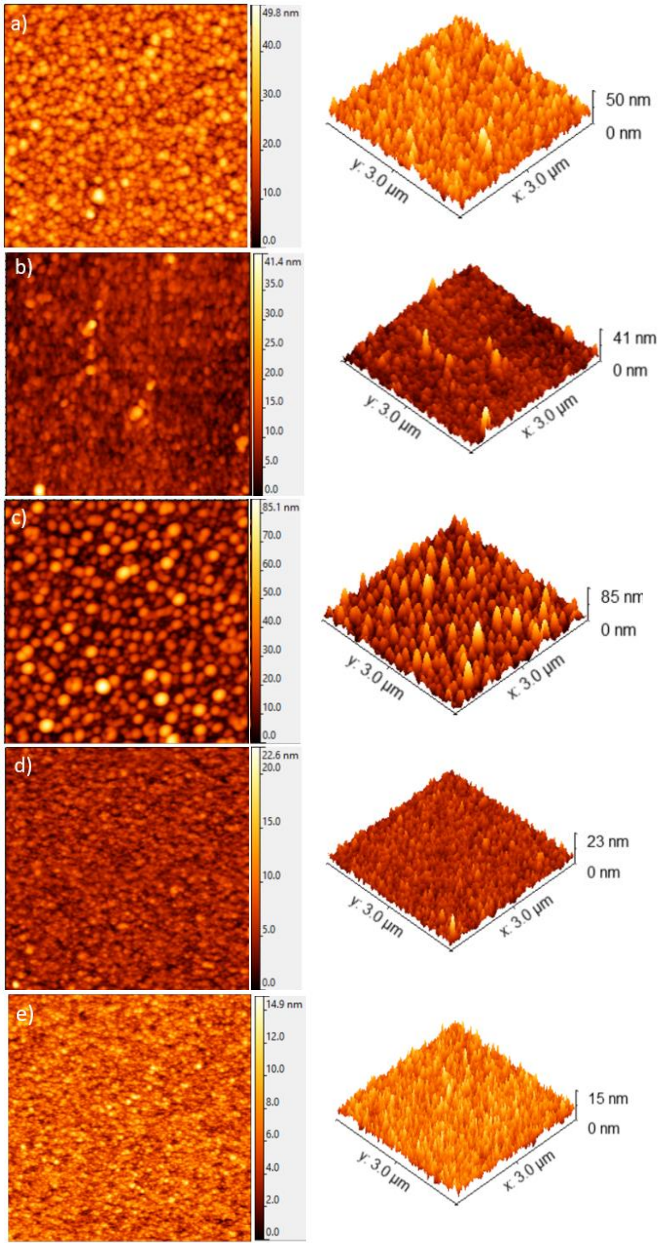

Figure 17. AFM images of 0.4 Pa films: a) ZrN-0.4-45; b) ZrN-0.4-300-30; C) ZrN-0.4-300-40; d) ZrN-0.4-300-80; e) ZrN-0.4-350-80.

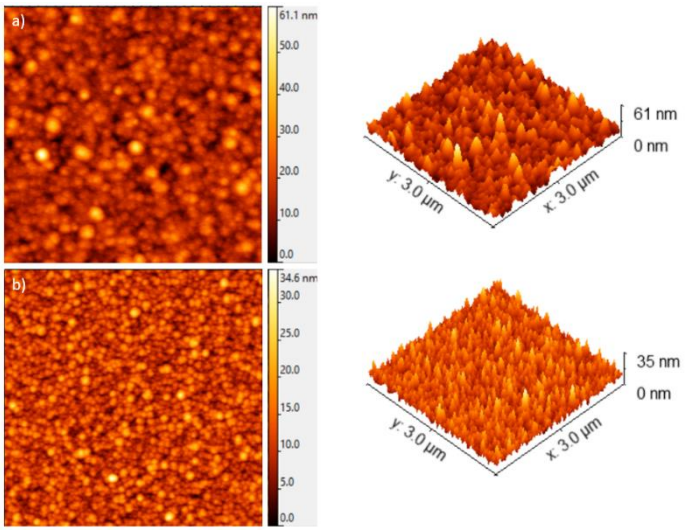

Figure 18. AFM images of 0.7 Pa films: a) ZrN-0.7-50; b) ZrN-0.7-250-50.

The topography also shows that the surfaces are mostly bumpy and have more peaks than depts (valleys), which is known by the values of kurtosis and skewness. For higher values of kurtosis, the surface becomes spikier and if the skewness was negative, it would present more depths than peaks (Maculotti et al., 2022) (see Table 8 and 9).

Table 8 – Roughness and porosity parameters of 0.4 Pa films.

	Mean roughness, Sa (nm)	Root mean square roughness, Sq (nm)	Skewness	Kurtosis
ZrN-0.4-45	5	6	0.4	0.4
ZrN-0.4-300-30	2	3	2	12
ZrN-0.4-300-40	7	10	2	4
ZrN-0.4-300-80	1	2	0.4	0.4
ZrN-0.4-350-80	1	2	0.5	0.4

Table 9 – Roughness and porosity parameters of 0.7 Pa films.

	Mean roughness, Sa (nm)	Root mean square roughness, Sq (nm)	Skewness	Kurtosis
ZrN-0.7-50	5	6	1	3
ZrN-0.7-250-50	3	4	1	0.8

4.1.4. Wettability

The contact angle (CA) measurements were brought out using four different liquids – α-bromonaphthalene (γ^d = 44.4 mN/m; γ^p = 0.0 mN/m), ultrapure water (γ^d = 19.9 mN/m; γ^p = 52.2 mN/m), glycerol (γ^d = 21.2 mN/m; γ^p = 41.5 mN/m), and brine (γ^d = 41.5 mN/m; γ^p = 31.7 mN/m) (Castro et al., 2022). For this study, since the coatings will be constantly exposed to sea water, the most significant analysis will be the interaction of the surface with brine. Surface free energy was calculated by the OWRK model (Castro et al., 2022) applied to coated surfaces, always keeping drop volumes below 10 µl to avoid the liquid weight influence. Figures 19 and 20 present all contact angles images with brine and Tables 10 and 11 display the values of contact angles and surface free energy.

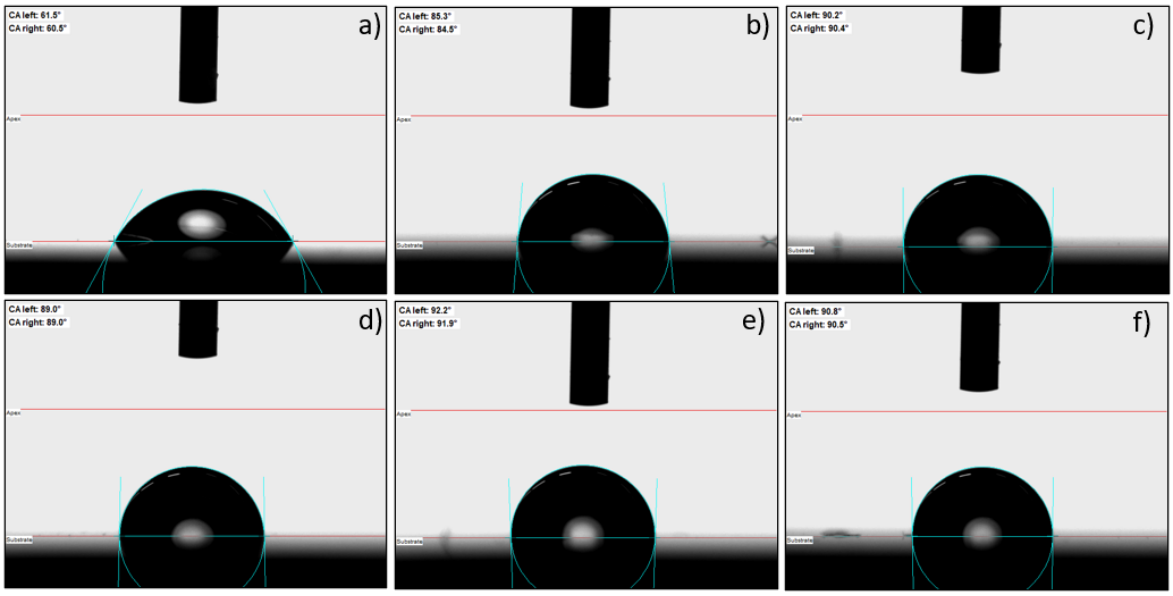

Figure 19. Contact angles images of uncoated stainless steel and all coatings deposited at 0.4 Pa: a) SS 316 L; b) ZrN-0.4-45; c) ZrN-0.4-300-30; d) ZrN-0.4.300.40; e) ZrN-0.4-300-80; f) ZrN-0.4-350-80.

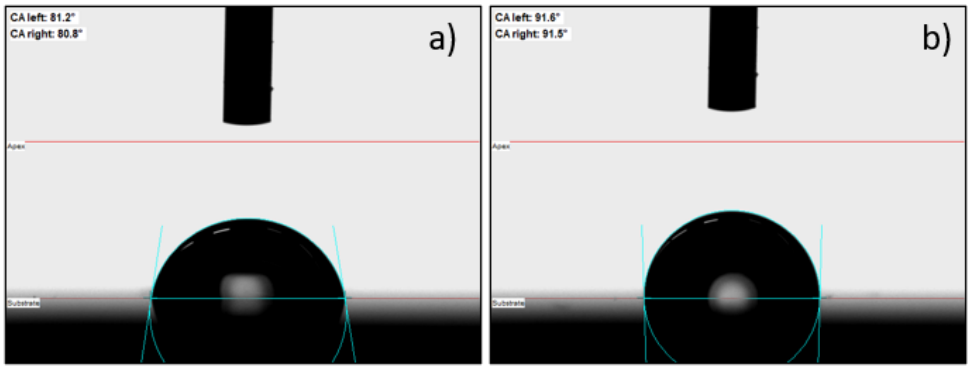

Figure 20. Contact angle images of coatings deposited at 0.7 Pa: a) ZrN-0.7-50; b) ZrN-0.7-250-50

The coatings can have a hydrophilic or hydrophobic behaviour, being hydrophilic when the contact angle is less than 90º and hydrophobic when it is over 90º (Yi et al., 2019). All HiPIMS films present a behaviour that is in the limit between hydrophilic and hydrophobic, since the contact angles were between 89º and 93º, being ZrN-0.4-300-80, ZrN-0.4-350-80, and ZrN-0.7-250-50 hydrophobic. On the other hand, DCMS films present a hydrophilic behaviour, with contact angles of 81º and 85º. Since these coatings have a columnar growth, the drop of artificial seawater easily penetrates the surface. The uncoated stainless steel is considerable hydrophilic as well, with 61º of brine contact angle, which proves the better properties of the coatings in this matter, as seen in figure 20. With α-bromonaphthalene, the coatings have CA values between 20º and 50º, which means that the surface is oleophilic (Castro et al., 2022) (Table 10 and 11).

According to the ORWK model, the surface free energy (SFE) can be divided in two components: polar and dispersive. The wettability can be characterized by the affection of the liquid to the solid surface. This implies that if the liquid has a polar and dispersive component identic to the solid's, the compatibility is high, leading to low contact angles and the surface would be wetted. A polar liquid will not facilitate the wetting of a non-polar surface, indicating high contact angles (Castro et al., 2022). All DOMS coatings displayed dispersive components between 35 – 38 mN/m, and the surface polar component had values between 2 – 6 mN/m (Table 10 and 11). These values differ from the brine surface tension values (γ^d = 41.5 mN/m; γ^p = 31.7 mN/m) and it can explain why the contact angles indicate a slight hydrophobic behaviour since the compatibility between the solid-liquid interface involves both components of surface free energy. Regarding the stainless steel (uncoated substrate), the polar component is slightly more intense compared to the coatings, resulting in a higher affinity with the artificial seawater and hence, to be wetted by this easily (meaning in lower CA values). Overall, DOMS coatings deposited with 80% of nitrogen flow (ZrN-0.4-300-80 and ZrN-0.4-350-80), plus DOMS at 0.7 Pa (ZrN-0.7-250-50), represent the most hydrophobic surfaces (Table 10 and 11).

Table 10 – Brine contact angles and surface free energy components of 0.4 Pa films and uncoated substrate.

	Brine CA (º)	SFE_d (mN/m)	SFE_p (mN/m)
SS 316 L	61 ± 2	34	9
ZrN-0.4-45	85 ± 1	36	3
ZrN-0.4-300-30	89 ± 2	37	3
ZrN-0.4-300-40	89 ± 2	38	6
ZrN-0.4-300-80	90 ± 3	38	2
ZrN-0.4-350-80	91 ± 2	35	2

Table 11 – Brine contact angles and surface free energy components of 0.7 Pa films and uncoated substrate.

	Brine CA (º)	SFE_d (mN/m)	SFE_p (mN/m)
SS 316 L	61 ± 2	34	9
ZrN-0.7-50	81 ± 1	41	2
ZrN-0.7-250-50	92 ± 1	36	3

The wettability is usually associated with the roughness, however, since in the present study all coatings exhibited low roughness values, this was not relevant to influence this property.

4.2. Mechanical behaviour

4.2.1. Adhesion strengh

The adhesion strength of the coatings was evaluated by scratch tests performed with a progressive load, as above-mentioned. Figures 21 exhibits the scratch images indicating the failure modes occurring at each critical load. Table 12 and 13 shows the values of the different critical loads. The failure modes in the coatings can be distinguished by cohesive or adhesive failure. The fist critical load, L_{c1}, is associated with the minimal load in which the coating suffers a cohesive failure; the second, L_{c2}, for the first adhesive failure and the third critical load, L_{c3}, is characterized by the removal of 50% of the film from the substrate (Carvalho, 2004).

As the scratch standard states, there are several types of cohesive and adhesive failures. In this case, L_{c1} represents a cohesive failure of conformal cracks, which is the film trying to adapt to the shape of the scratch groove and produce arcs that open from the direction of scratching (Fig. 21a). L_{c2} shows an adhesive failure of buckling when the coating buckles ahead of the tip and starts to slightly detach from the substrate (Fig. 21b). Finally, L_{c3} is when the coating separates 50% of the substrate as afore mentioned (Fig. 21c) (*ASTM C1624-05*, 2010).

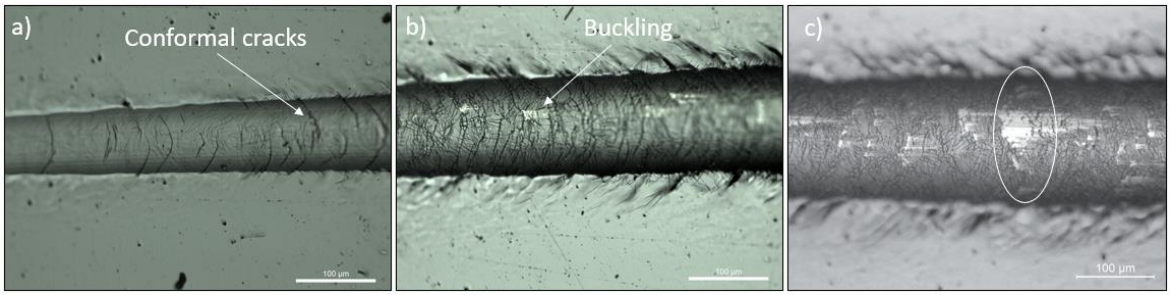

Figure 21. Example of scratch parts representing each critical load a) L_{c1}; b) L_{c2}; c) L_{c3}.

With the values of critical loads (Tables 12 and 13), it is possible to assume that the DCMS films seem to have a better adhesion strength, since the critical loads are superior, which means that the film can support higher forces until detaching from the substrate or beginning to show failure. However, the DOMS coating deposited with 80% of nitrogen flow and deposited at 0.4 Pa working pressure (ZrN-0.4-300-80), also states a high value of the third critical force, L_{c3}. Usually, high values of residual compressive stresses are associated with low critical loads, which is seen in some films such as ZrN-0.4-300-30, ZrN-0.4-300-40, and ZrN-0.7-250-50, but it is not a linear pattern through all the samples regarding the adhesion/stress relationship, thus, it cannot be concluded that the adhesion depends directly on this. The adhesion strength can be correlated with many factors such as the thickness, friction coefficient, interfacial properties, as well as the residual stresses created along the film growth and the surface state of the substrate (Carvalho, 2004).

Table 12 – Critical loads values for films obtained at 0.4 Pa.

	L_{c1} (N)	L_{c2} (N)	L_{c3} (N)
ZrN-0.4-45	7 ± 1	24 ± 0	43 ± 5
ZrN-0.4-300-30	3 ± 1	10 ± 0	22 ± 2
ZrN-0.4-300-40	5 ± 0	12 ± 2	24 ± 5
ZrN-0.4-300-80	7 ± 2	22 ± 4	41 ± 1
ZrN-0.4-350-80	6 ± 0	18 ± 3	29 ± 5

Table 13 – Critical loads values for films obtained at 0.7 Pa.

	L_{c1} (N)	L_{c2} (N)	L_{c3} (N)
ZrN-0.7-50	8 ± 1	19 ± 3	37 ± 3
ZrN-0.7-250-50	4 ± 0	13 ± 2	21 ± 3

4.2.2. Residual Stresses and Hardness

The residual stresses were calculated by the Stoney equation as describe in 3.4.2., which are represented in Tables 14 and 15. At first sight, all films present compression stresses, which is usual in films deposited by reactive magnetron sputtering technology, since the high energy bombardment creates defects in the structure and film growth (Carvalho, 2004). Also, in the coatings deposited at 0.4Pa, as the deposition rate decreases, the residual stress decreases as well. This is mainly evident in the coatings with 80% of nitrogen flow, which are the least efficient in the process. However, at 0.7Pa for DOMS, the behaviour was the opposite since the deposition rate decreases and the residual stress rises.

Table 14 – Compressive Residual stress of 0.4 Pa films.

	Compressive Residual stress (GPa)
ZrN-0.4-45	2 ± 0.6
ZrN-0.4-300-30	2 ± 0.2
ZrN-0.4-300-40	2 ± 0.1
ZrN-0.4-300-80	1 ± 0.1
ZrN-0.4-350-80	1 ± 0.2

Table 15 – Compressive Residual stress of 0.7 Pa films.

	Compressive Residual stress (GPa)
ZrN-0.7-50	1 ± 0.5
ZrN-0.7-250-50	3 ± 0.1

Figures 22 and 23 exhibit the relationship between compression residual stresses and hardness of the coatings deposited at 0.4Pa and 0.7Pa, respectively. As the nitrogen flow increases, the hardness tends to increase as well, however the residual stress, on the other hand, decreases. ZrN-0.4-300-80 has the highest hardness (25 GPa) with low compressive stress of 1 GPa, which could be considered a hard film with low residual stresses. At 0.7 Pa of working pressure, it is seen a different behaviour: the coating deposited by DOMS presents the same value of hardness as the DCMS film, but a considerably higher residual compressive stress (Fig. 23), which indicates that the compression stresses do not have a significant influence in hardness in this case. Possibly, this variation in stresses could be connected to the nature of HiPIMS processing itself at the ZrN-0.7-250-50 sample conditions or related to the structure. Nonetheless, every coating exhibited low values of residual stresses, when compared to other studies regarding ZrN films (Zhang et al., 2007) (Purandare et al., 2011).

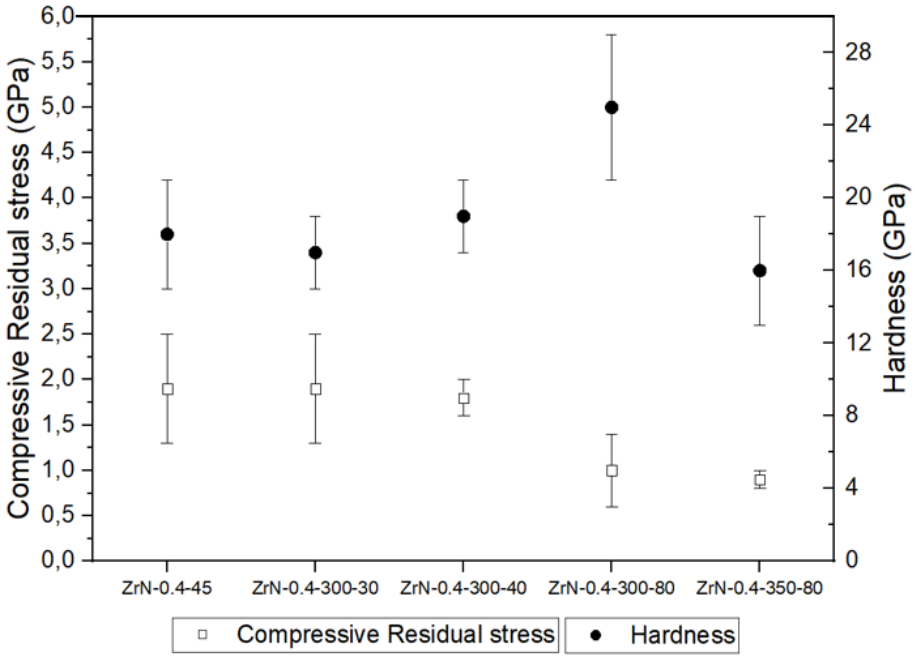

Figure 22. Residual stresses and hardness of 0.4 Pa films.

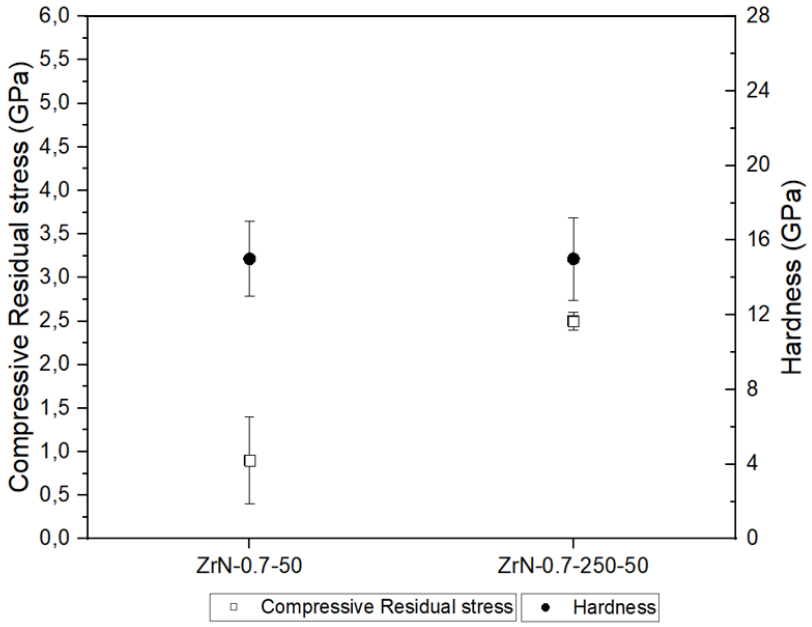

Figure 23. Residual stresses and hardness of 0.7 Pa films.

Tables 16 and 17 exhibit the values of hardness, young's modulus, H/E ratio and the indentation maximum depth of every coating. In the films deposited at 0.4 Pa and 300V by DOMS, the indentation depth was kept lower than 10% of the coating thickness, thus the substrate did not influence the measurements. However, in some of the other films there was not possible to avoid the substrate's effect completely. In general terms, the hardness of the films deposited by DOMS was higher than by DCMS and it is seen a slight trend of hardening as the nitrogen rises in the films obtained at 0.4 Pa working pressure and 300 V DC_{int}. However, the main difference is in the ZrN-0.4-300-80 film, which shows a significant increase in hardness, being a film that is very dense and oriented in (220) ZrN structure, which is described in the literature has a common behaviour in films subjected to high energy bombardment (Ferreira et al., 2016).

Some authors report that the tensile stresses decrease the nanoindentation hardness and compressive stresses increase it (Ferreira et al., 2014), which is why the hardness of every ZrN film deposited is relatively high since all residual stresses are compressive. These compressive stresses are due to the high energy delivered by bombardment ions as the films grows which influences the mechanical properties, increasing hardness and reflecting on the phase composition (Musil et al., 2016) Also, for denser films the hardness tends to be higher as it is proven in dense DOMS coatings such as ZrN-0.4-300-80 (Ferreira et al., 2016).

Hardness is a property that provides indications of the resistance when it comes to plastic deformation. Yet, the mechanical behaviour of the coatings does not only depend on hardness, but it is also characterized by the Young's modulus (Carvalho, 2004). In this matter, the ratio H/E is important to look at (Tables 16 and 17). A high H/E value was seen in ZrN-0.4-300-80 with 80% of nitrogen flow during deposition, 0.1, which indicates better resistance to plastic deformation, and it is also related to the better adhesion strength seen by a high value of the third critical load (Table 12), indicating a good resistance to cracking (Musil et al., 2016). On the other hand, the films obtained by DCMS exhibited the lower H/E ratio values which could mean worser abrasive wear contact and hence, poorer performance of these coatings to the abrasive behaviour provoked by the sand inside the seawater (Boxman et al., 2007).

Table 16 – Hardness, Young's modulus and H/E ratio of films obtained at 0.4 Pa.

	Hardness, H (GPa)	Young's modulus, E (GPa)	H/E	Indentation depth, h (nm)
ZrN-0.4-45	18 ± 3	285	0.06	104 ± 5
ZrN-0.4-300-30	17 ± 2	231	0.07	111 ± 5
ZrN-0.4-300-40	19 ± 2	246	0.08	103 ± 5
ZrN-0.4-300-80	25 ± 4	242	0.10	104 ± 8
ZrN-0.4-350-80	16 ± 2	222	0.07	119 ± 6

Table 17 – Hardness, Young's modulus and H/E ratio of films obtained at 0.7 Pa.

	Hardness, H (GPa)	Young's modulus, E (GPa)	H/E	Indentation depth, h (nm)
ZrN-0.7-50	15 ± 2	261	0.06	114 ± 6
ZrN-0.7-250-50	15 ± 2	245	0.06	117 ± 6

The coating with the highest hardness also presents a higher value of the lattice parameter (4.64 Å). This phenomenon means that the lattice of the crystalline structure is submitted to compression forces, probably because of the high energy induced in deposition that displaces atoms for interstitial positions in the lattice that provoke compressive stresses (Carvalho, 2004). This increased hardness with a larger lattice parameter has been reported

by other authors (Ferreira et al., 2016), and it could also be related to the highly crystalline ZrN structure in ZrN-0.4-300-80, whereas the other films could have some oxygen dopped in the lattice which decreases the crystallinity (Carvalho et al., 2005), although in this study there was not detected enough oxygen.

4.3. Functional behaviour

4.3.1. Corrosion

The corrosion behaviour of the ZrN coatings and uncoated stainless-steel SS 316 L were characterized by potentiodynamic polarization (PP) and EIS measurements, obtaining the corrosion potential and electrochemical response of the films. The parameters obtained from PP – βa, βc, I_{corr}, E_{corr}, and corrosion rate – are exhibited in Table 18 and plots in Figure 24.

Uncoated stainless steel clearly displayed the worst corrosion behaviour in comparison with all ZrN coatings, which is visible in the polarization curves, being the only material that shows some pitting events at higher potentials (Fig. 24). ZrN-0.4-300-80 showed a corrosion rate 4 times lower than stainless steel (Table 18), which means a remarkable improvement to resist the seawater action. This film represents the best anticorrosive performance when it comes to Icorr and corrosion rate. The coatings proved to be more noble than SS, especially those deposited by DOMS.

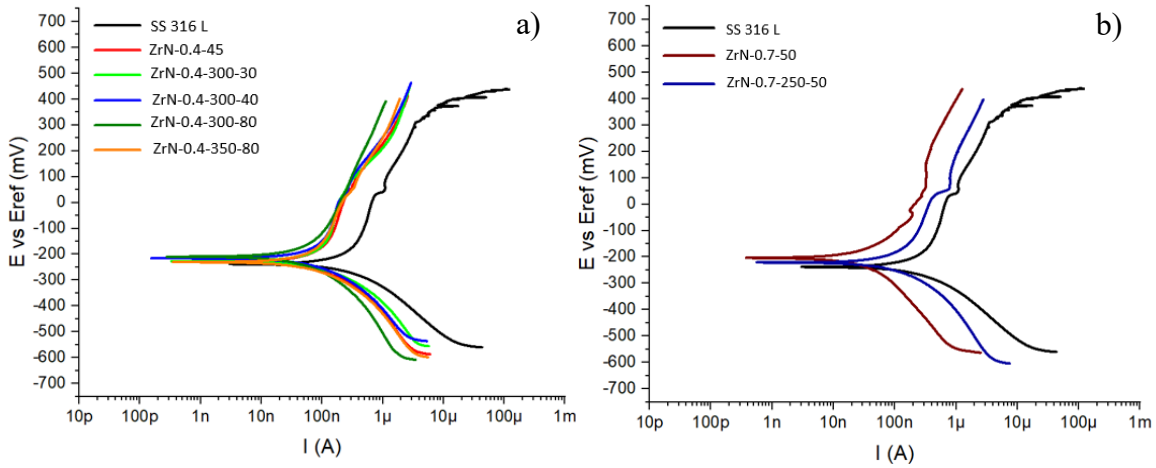

Figure 24. Tafel curves obtained by PP testes: a) 0.4 Pa films; b) 0.7 Pa films.

This analysis indicates that all coatings showed an improvement in electrochemical performance in artificial seawater exposure according to the PP tests. Stainless steel is known to be good corrosion resistance material, which builds a chromium oxide protective outermost layer, but it is not mechanically resistant, hence it does not provide an effective protection. As the nitrogen increased in the films, the corrosion rates were smaller and hence, better the anticorrosion behaviour (Table 18). This was expected, because ceramic coatings commonly show this behaviour and, as the nitrogen increases, the less metallic the material is, hence more ceramic.

Also, the morphology of DOMS films exhibited dense coatings, and AFM showed low roughness and porosity levels, which is directly related to the corrosion resistance, by not allowing for the penetration of the electrolyte to the substrate. Besides, the chemical composition and wettability highly influences the electrochemical behaviour as well. Coatings with higher contact angles with brine are those that exhibited the lower corrosion rates, being ZrN-0.7-250-50 the worst, which can be explained by the fact that the morphology of the film shows a columnar growth, seen in SEM images, which implicates that it would be easily affected.

Table 18 – Fit parameters of potentiodynamic polarization curves of ZrN coatings.

	β_a (mV/decade)	β_c (mV/decade)	I_{corr} (nA)	E_{corr} (mV)	Corrosion rate ($x10^{-3}$mm/yr)
SS 316 L	365 ± 113	121 ± 2	277 ± 14	-248 ± 10	10.2 ± 0.5
ZrN-0.4-45	458 ± 56	281 ± 46	396 ± 7	-255 ± 4	7.8 ± 0.1
ZrN-0.7-50	1832 ± 424	1014 ± 245	284 ± 4	-186 ± 18	5.7 ± 0.1
ZrN-0.4-300-30	1056 ± 510	210 ± 108	149 ± 32	-255 ± 8	2.8 ± 0.6
ZrN-0.4-300-40	1412 ± 637	221 ± 46	150 ± 32	-214 ± 1	2.8 ± 0.6
ZrN-0.4-300-80	1074 ± 68	255 ± 47	138 ± 2	-212 ± 2	2.5 ± 0
ZrN-0.4-350-80	1397 ± 310	182 ± 12	143 ± 5	-227 ± 2	2.6 ± 0.1
ZrN-0.7.250.50	744 ± 171	209 ± 17	222 ± 6	-217 ± 5	4.3 ± 0.1

SEM images after corrosion PP tests were taken to see the defects appearing in the surface and identify what kind of corrosion occurred. Figure 25 exhibits a SEM image of the defects generated by corrosion found in one of the films, as well as EDS spectra of chemical

composition. Zone (a) represents a zone with no defects, whereas zone (b) exhibits some pitting, which leads to a small failure of the film in zone (c), where the localized defects progressively led to the creation of small holes in the surface. The EDS results showed a slight absorption of oxygen as the failure in the film appears. In Figure 25 the chemical composition of the zone with no corrosion detected displays 4 at% of oxygen, meanwhile the pitting zone showed 5 at% of oxygen. The mapping of the film is exhibited in Figure 26 which also shows the NaCl deposits. Despite this, the overall surface did not present many corrosion phenomenon, only localized defects, which does not affect the corrosion resistance in this case.

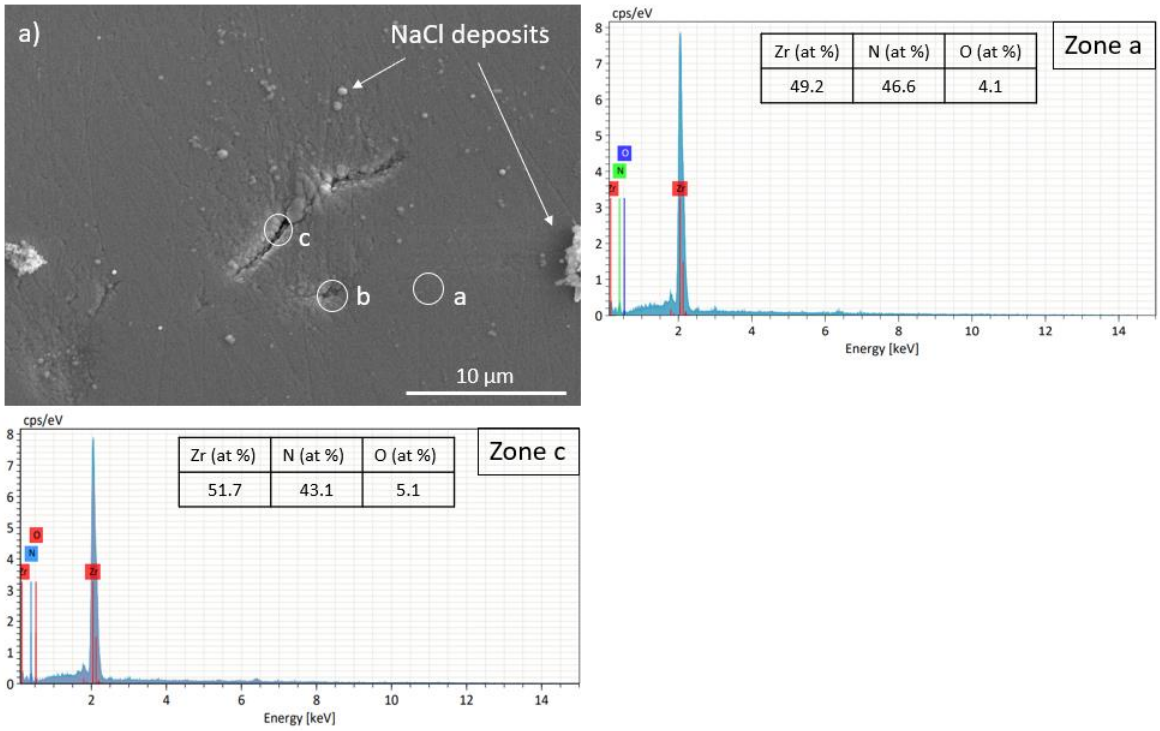

Figure 25. SEM image after corrosion of ZrN-0.4-300-30 and EDS scans of the zone (a) and (c) represented in the image.

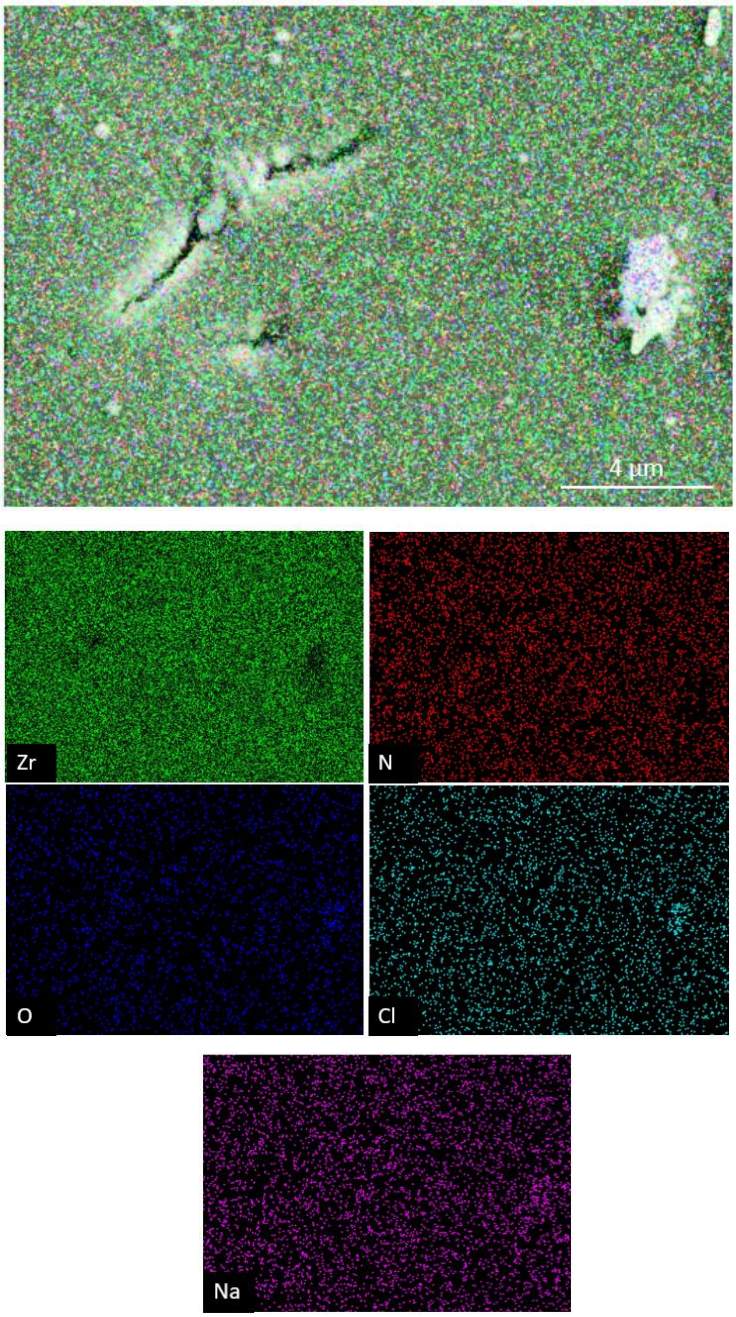

Figure 26. Mapping of the corroded ZrN-0.4-300-30 (figure 28).

Results from EIS measurements are exhibited in Figures 27 and 28. The Bode plots (Figure 27) revealed the presence of a one-time constant at the intermediate frequency zone, indicating that there is no diffusion process, therefore there is no Warburg element. Some authors have described that the appearance of one-time constant is common for non-porous coatings, avoiding the creation of a diffusion path for the corrosive agents, in contrast of

what happens in porous coatings (Mejía et al., 2022). This also indicates that there are no other layers formed on top of the coating.

The coatings displayed small variation over time, only stainless-steel exhibited a slight change. Concerning the impedance modulus, Z_{mod}, ZrN-0.4-300-80 exhibits the highest value, implying a better corrosion resistance and, on the other hand, ZrN-0.7-50 and SS display the lowest values. As higher nitrogen content in the film, this becomes more ceramic, which increases the corrosion resistance by showing a higher impedance modulus. DCMS coatings show lower impedance modulus when compared to DOMS, indicating worse electrochemical properties, supporting the results from PP. Nyquist plots (Figure 28) proof that there is no diffusion process since the semi-circle is always stable and wide. As it reaches 168h of exposure, there are no significant changes or high decrease in Z_{mod}.

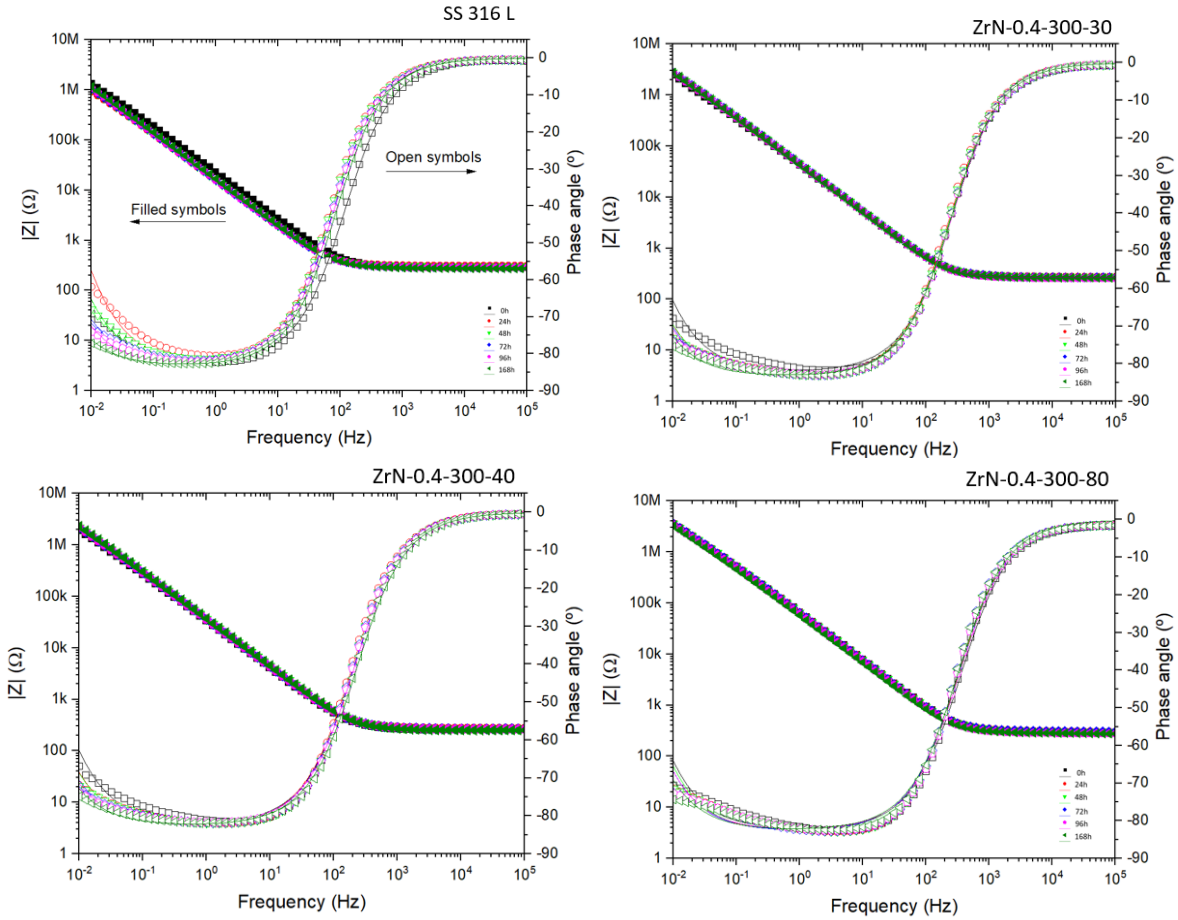

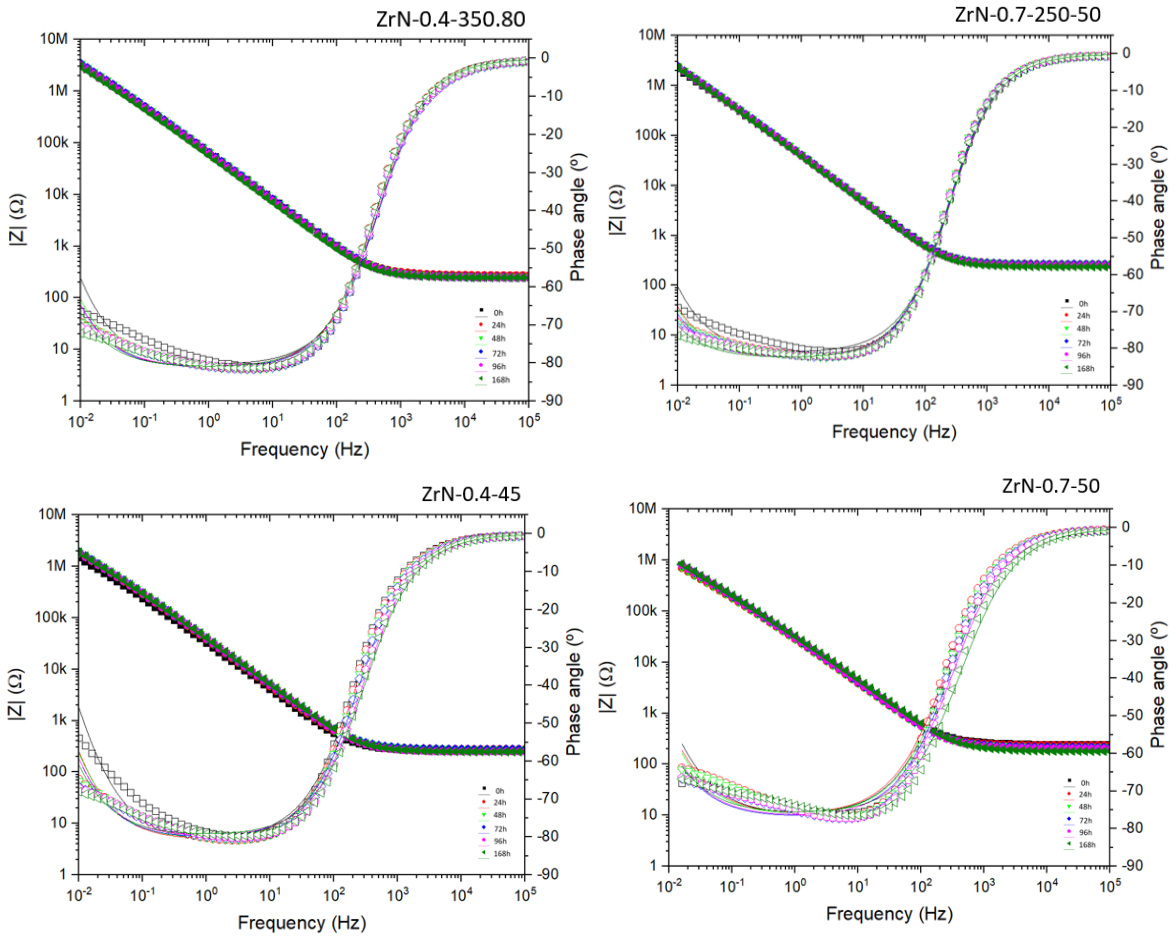

Figure 27. EIS bode plots of ZrN coatings and uncoated SS from 0h to 168h of artificial sewater exposure.

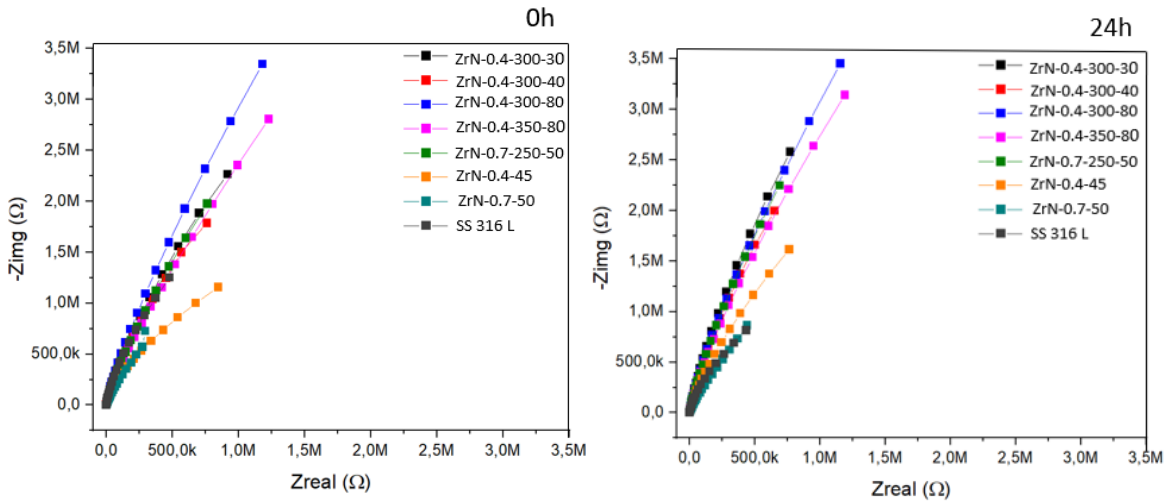

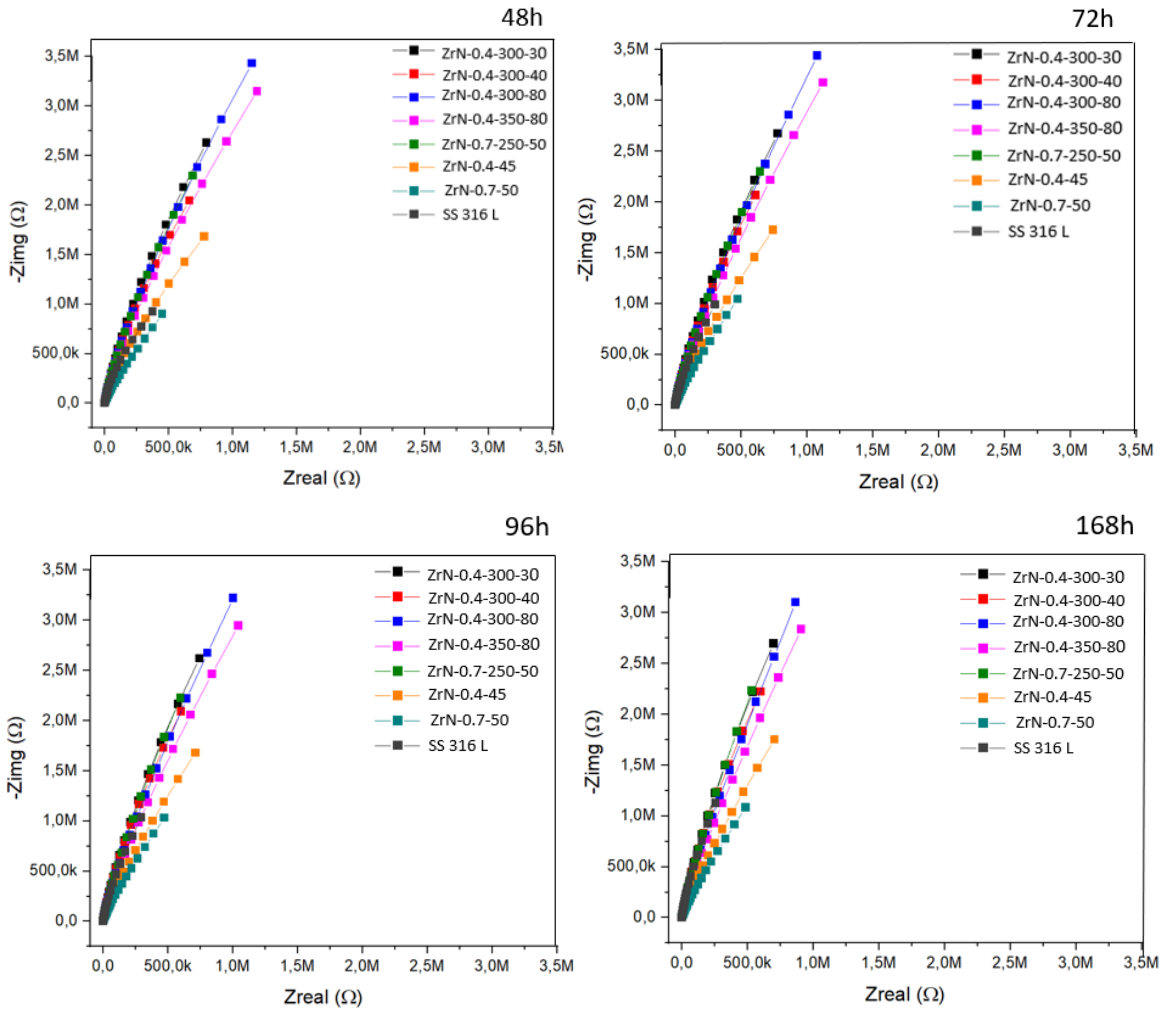

Figure 28. Nyquist plots of ZrN coatings and SS from 0h to 168h of artificial seawater exposure.

The equivalent electric circuit (EEC), used to fit all the EIS measurements, is represented in Figure 29. This process always kept the chi-square value in the order of 10^{-3}, representing a good fit according to some authors (Cubillos et al., 2021). The circuit is constituted by R_{sol}, the resistance of the solution, R_{coat}, the resistance of the coating, and CPE_{coat}, the constant phase element of the coating. This last one, presented in parallel with the coating resistance, is applied to fit the electrochemical response of the surface, indicating that the film is a non-ideal capacitor, due to the presence of some heterogeneities (Castro et al., 2022). CPE is accompanied by a constant phase exponent, α (sometimes described as *n*). The values of α can vary among 0 and 1. Closer to 1 means that the surface has less defects and the material becomes more like a pure capacitor. On the contrary, values close to 0

represent the appearance of more impurities and defects and a behaviour close to resistance (Cubillos et al., 2021). The ZrN coatings deposited by DOMS displayed an exponent around 0.9, which indicates a surface with few defects and impurities, and DCMS films exhibit slightly lower values, 0.86 (see Table 19), indicating the existence of higher amount of surface impurities and a less capacitor behaviour. The low values of roughness and porosity as well as the dense morphology of HiPIMS coatings and high contact angles with seawater influenced this behaviour. The fit parameters obtained from EIS plots are exposed in Table 19.

Table 19 – Fit parameters of EIS according to the equivalent electric circuit.

	R_{sol} (Ω)	R_{coat}(MΩ)	CPE_{coat}(μS*s^{α})	α
SS 316 L	289 ± 15	4 ± 1	11 ± 1.3	0.90 ± 0.02
ZrN-0.4-45	270 ± 14	4 ± 1	6 ± 0.2	0.86 ± 0
ZrN-0.7-50	228 ± 22	4 ± 1	9 ± 0.4	0.87 ± 0
ZrN-0.4-300-30	277 ± 12	10 ± 2	5 ± 0.1	0.90 ± 0
ZrN-0.4-300-40	279 ± 13	8 ± 2	6 ± 0.1	0.91 ± 0
ZrN-0.4-300-80	321 ± 17	10 ±1	4 ± 0.2	0.90 ± 0
ZrN-0.4-350-80	286 ± 15	10 ± 1	4 ± 0.2	0.90 ± 0
ZrN-0.7-250-50	271 ± 16	9 ± 2	5 ± 0.1	0.90 ± 0

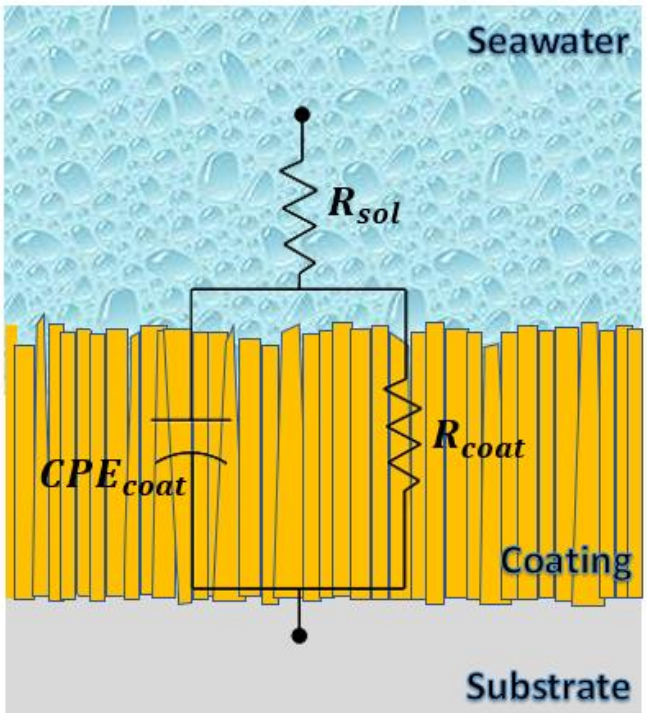

Figure 29. Equivalent Electric Circuit (ECC) of the ZrN coatings.

5. CONCLUSIONS

Anticorrosive ZrN coatings were successfully deposited by reactive magnetron sputtering. Chemical, physical, mechanical, and electrochemical properties were analysed. According to the initial objectives and demands on the film's properties defined in the beginning of the work, the main conclusions are:

- The increased densification in HiPIMS films was proven, where the slight increase of nitrogen in the ZrN chemical composition enhanced the dense morphology, unlike DCMS coatings that exhibited columnar growth. An overall thickness of 1µm was attained at almost every coating, although DOMS films showed a decrease in deposition rate.
- Crystalline structure exhibited phases of face cubic centred ZrN and hexagonal Zr, with a clear change in orientation from (111) to (220) plane (ZrN phase) as the nitrogen increased. DOMS coatings deposited with 80% of nitrogen flow displayed a structure oriented in the (220) plane and with no relevant presence of Zr phases, indicating the decrease in structural zirconium leading to a less metallic coating. The lattice parameter proved to be larger than the pattern's, as a result of compressive stresses and leading to a deviation of the pattern's line to lower 2Θ values.
- Surface roughness was low for all coatings, mainly in DOMS, without significance influence on functional properties. Surface free energy and contact angles with brine showed a closeness to hydrophobicity in DOMS films, whereas the DCMS films exhibited a hydrophilic behaviour as well as the SS substrate.
- Mechanical properties were characterized by hardness, residual stress and adhesion strength, where DOMS coatings showed a slight worse adhesion behaviour than those of DCMS. Nevertheless, ZrN-0.4-300-80 presented a good adhesion, accompanied by the highest hardness and a low residual stress value. All the films presented compressive residual stresses which values can be considered as low. Concerning the H/E ratio, ZrN-0.4-300-80 exhibited the highest value (~0.1) and possibly, the best abrasive wear contact resistance.
- Electrochemical analyses were brought out by EIS measurements up to 168h of artificial seawater exposure and PP tests at 0h. Every coating proved to be better than uncoated stainless steel, since Ecorr showed noble films and Icorr was lower, and

consequently lower corrosion rates. Once again, ZrN-0.4-300-80 proved to be the most resistant, indicating the lower corrosion rate. Also, the DCMS coatings had a lower value of α, implying more surface defects and impurities, unlike DOMS. Corrosion resistance was mainly influenced by the chemical composition, wettability, and the morphology.

There was one film that positively stood out in mechanical, chemical, and anticorrosive properties – DOMS deposited with 80% nitrogen flow, deposited with 300 V DC_{int} at 0.4 Pa working pressure, labelled as ZrN-0.4-300-80. This coating had the highest hardness, a dense morphology, hydrophobicity, lower corrosion rate and corrosion current density. In general, the DOMS films deposited at 0.4 Pa working pressure showed better behaviour than the coating deposited at 0.7Pa.

Summing up, the deposition of HiPIMS films improved the properties of the ZrN films. Even though the deposition rate was low in HiPIMS films, those demonstrated to be successful for the application in sea chest gratings. This will be a good base to build a multifunctional coating with antimicrobial properties.

6. SUGESTIONS FOR FUTURE WORK

Regarding the developed ZrN coatings by HiPIMS, the disadvantages are the low deposition rates and a slight worse adhesion strength. The adhesion could be improved by depositing the ZrN coating in a gradient mode above the Zr interlayer.

The main suggestion regards a part of this study that was not detailed because of the few time available. One of the initial objectives of this work concerning the functional characterization of the ZrN coatings, besides the corrosion analysis, was to perform erosion-corrosion tests. As these coatings will be submitted to the marine environment for a long period of time, the effect of erosion caused by the action of sand is also important to analyse.

In that matter, a prototype for erosion-corrosion tests was developed in the beginning of this thesis, to submit the samples of uncoated and coated stainless steel to the action of microparticles assembling sand, distributed in artificial seawater. The prototype is exhibit in figure 30, and a proposal for the sample holder in figure 31, in 3D design. This project was being carried out with the help of Instituto Pedro Nunes (IPN), that is responsible for the implementation of the system. However, the time available for the development of this thesis did not make it possible to implement and test the erosion-corrosion system, so it remains for the future work in the multifunctional coatings development for sea chest gratings.

Explaining the prototype, the particles mixed with artificial seawater are driven through the circuit in PVC tubes, with the use of a peristaltic pump with 2.7 W of power, 8mm piping diameter, and a flow of 2167 mL/min. These calculations were made to reach a speed of 11.5 m/s, which is reported in the literature as the usual speed of industrial transport ships and was already tested in erosion-corrosion tests by other authors (Bastidas, 2014). However, to obtain this, it is necessary to have a flow reductor, just after the sample holder, to reduce from 8mm to 2mm diameter, to reach the sample with the same flow. The value of flow was calculated by equation 5, being “1” the point before the reductor and “2”, the point after the reductor.

$$Q_1(d = 8mm) = Q_2(d = 2mm) <=> v_1 = v_2 \quad (4)$$

Where Q_1 and Q_2 are the flows in each point, respectively, as well as v_1 and v_2 are the speed of the solution in each point. From equation 5 and 6 results the value of flow and v_1.

$$Q_2\ (m^3/s) = v\ (m/s) x\ A\ (m^2) = 11.5\ x\ \pi(\frac{0.002}{2})^2 = 3.6x10^{-5}\ (m^3/s) \\ = 2167\ (mL/\text{min}\ ) \quad (5)$$

$$v_1 = \frac{11.5\ x0.002}{0.008} = 0.72\ \ (m/s) \quad (6)$$

The power of the pump was calculated based in the Bernoulli equation:

$$\frac{p_1}{\rho g} + z_1 + \frac{{v_1}^2}{2g} + H_b - h_t = \frac{p_2}{\rho g} + z_2 + \frac{{v_2}^2}{2g} \quad (7)$$

Since both pressures are equal (atmospheric pressure), considering $z_1$the 0 point and z_2 the point at the water line of 10 cm (the height from the bottom of the reservoir to the water line) and $v_1 = 0$, the equation takes the form of:

$$H_{pump} = z_2 + \frac{{v_2}^2}{2\ g} + h_t \quad (8)$$

Where H_{pump} is the pump's head, g is the gravity's acceleration, and h_t represent the system's losses, which are divided in primary and secondary losses. Primary losses are calculated with the Darcy equation and the secondary are related to the accessories used in the system (reductor, Tee, valves, and unions). After calculating the loss of 0.75, the pump's head was determined. With that value, the power of the pump, P_{pump}, results from equation 10.

$$H_{pump} = 0{,}1 + \frac{11.5^2}{2x9.81} + 0.75 = 7.6\ m \quad (9)$$

$$P_{pump} = \rho g H_{pump} Q = 998.2\ x\ 9.81\ x\ 7.6\ x\ 3.6\ x\ 10^{-5} \\ = 2.7\ W \quad (10)$$

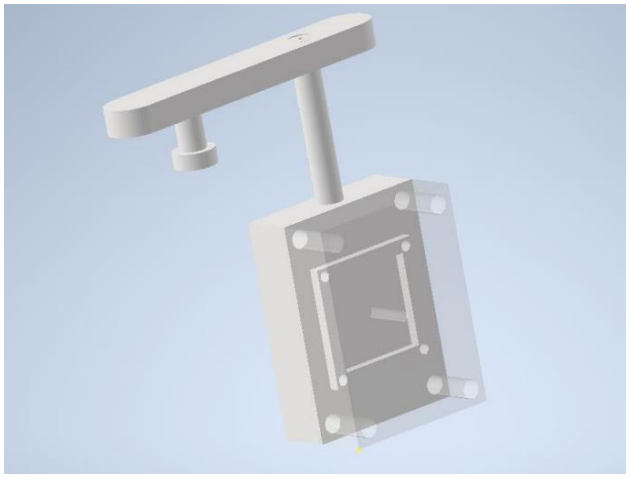

Figure 30. 3D design of the proposed sample holder.

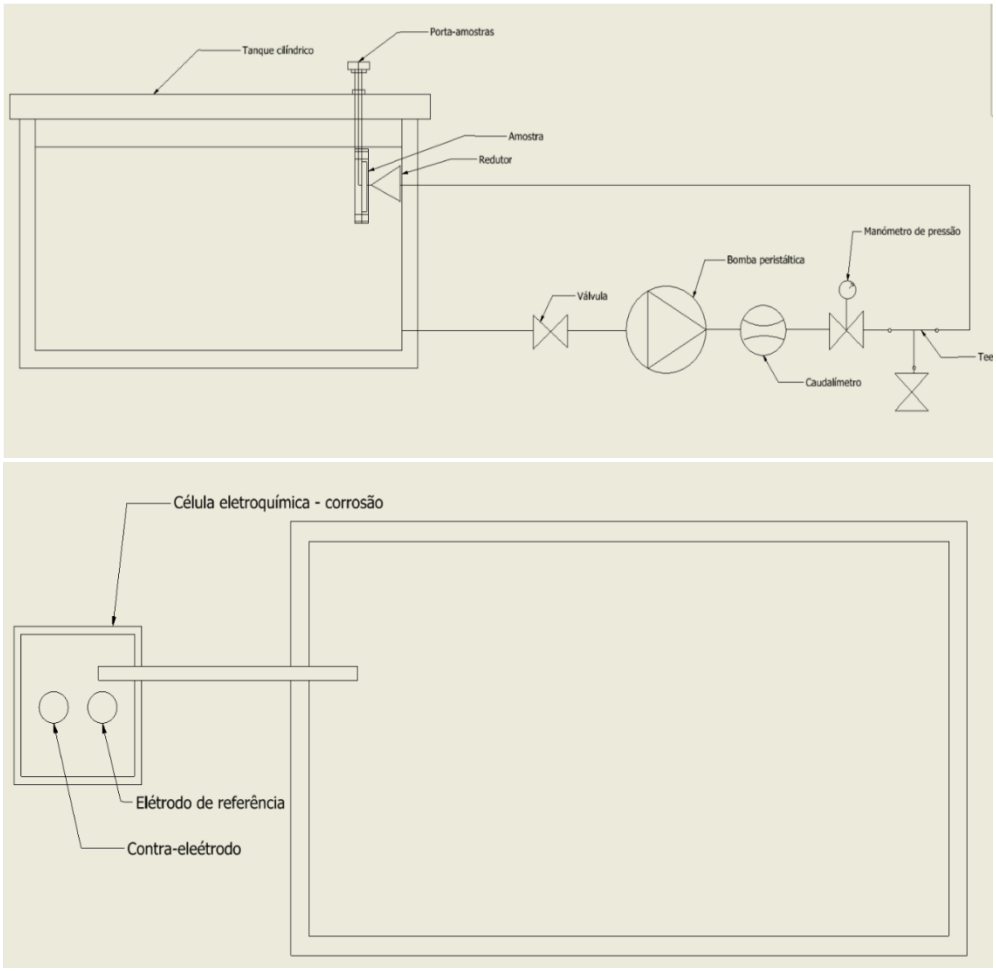

Figure 31. 2D view of the prototype designed for erosion-corroion tests (bottom drawing representing the connection of the reservoir to the electrochemical cell for the corrosion part).

BIBLIOGRAPHY

[1] https://amarineblog.com/2017/07/27/mgps-marine-gross-protection-system/.

[2] https://www.quora.com/On-a-ship-or-boat-what-is-a-sea-chest.

Anders, A. (2010). "A structure zone diagram including plasma-based deposition and ion etching." *Thin Solid Films*, *518*(15), 4087–4090. https://doi.org/10.1016/j.tsf.2009.10.145

Anders, A. (2017). "Tutorial: Reactive high power impulse magnetron sputtering (R-HiPIMS)." *Journal of Applied Physics*, *121*(17). https://doi.org/10.1063/1.4978350

ASTM C1624-05. (2010). "Standard test method for adhesion strength and mechanical failure modes for ceramic coatings by quantitative single point scratch testing." American Society for Testing and Materials International, United States. https://doi.org/10.1520/C1624-05R10

ASTM G102-89. (1999). "Standard practice for calculation of corrosion rates and related information for electrochemical measurements." American Society for Testing and Materials, United States.

Baptista, A., Silva, F., Porteiro, J., Míguez, J., & Pinto, G. (2018). "Sputtering physical vapour deposition (PVD) coatings: A critical review on process improvement andmarket trend demands." In *Coatings* (Vol. 8, Issue 11). MDPI AG. https://doi.org/10.3390/COATINGS8110402

Bastidas, F. (2014). "Erosión Corrosión de recubrimientos ternarios de carburos de Vanadio-Niobio depositados mediante la técnica TRD sobre aceros AISI H13 y AISI D2." Master Thesis in Materials and Processes, Mechanical and Mechatronics Engineering Department, National University of Columbia

Benea, L., Mardare, L., & Simionescu, N. (2018). "Anticorrosion performances of modified polymeric coatings on E32 naval steel in sea water." *Progress in Organic Coatings*, *123*, 120–127. https://doi.org/10.1016/j.porgcoat.2018.06.020

Bianca Castanheira Caratão. (2014). "Desenvolvimento e fabrico de estruturas para aplicações biomédicas por *electrospinning*" Master thesis in Material's Engineering, University of Minho.

Boxman, R., Veprek, S., Zhitomirsky, V., & Raveh, A. (2007). "Superhard Coatings". www.hardcoat.org.

Carvalho, P. (2008). "Development of new decorative coatings based on zirconium oxynitrides." Doctoral thesis in Science – Physics, University of Minho.

Carvalho, P., Vaz, F., Rebouta, L., Cunha, L., Tavares, C. J., Moura, C., Alves, E., Cavaleiro, A., Goudeau, P., le Bourhis, E., Rivìre, J. P., Pierson, J. F., & Banakh, O. (2005). "Structural, electrical, optical, and mechanical characterizations of decorative ZrO xN y thin films." *Journal of Applied Physics*, *98*(2). https://doi.org/10.1063/1.1990261

Carvalho, S. (2004). "Propriedades mecânicas e características microestruturais de filmes finos nanocompósitos de (Ti,Al,Si)N preparados por pulverização catódica reactiva em magnetrão." Doctoral thesis in Science – Physics, University of Minho.

Castro, J. D. (2020). "Multifunctional coatings for antibiofouling applications." Doctoral thesis plan in Materials Engineering, University of Minho.

Castro, J. D., Lima, M. J., & Carvalho, S. (2022). "Wetting and corrosion properties of CuxOy films deposited by magnetron sputtering for maritime applications." *Applied Surface Science*, *584*. https://doi.org/10.1016/j.apsusc.2022.152582

Chambers, L. D., Stokes, K. R., Walsh, F. C., & Wood, R. J. K. (2006). "Modern approaches to marine antifouling coatings." *Surface and Coatings Technology*, *201*(6), 3642–3652. https://doi.org/10.1016/j.surfcoat.2006.08.129

Cubillos, G. I., Romero, E., & Umaña-Perez, A. (2021). "ZrN-ZrOxNy vs ZrO2-ZrOxNy coatings deposited via unbalanced DC magnetron sputtering." *Scientific Reports*, *11*(1). https://doi.org/10.1038/s41598-021-98052-2

Elmkhah, H., Attarzadeh, F., Fattah-alhosseini, A., & Kim, K. H. (2018). "Microstructural and electrochemical comparison between TiN coatings deposited through HIPIMS and DCMS techniques." *Journal of Alloys and Compounds*, *735*, 422–429. https://doi.org/10.1016/j.jallcom.2017.11.162

Ferrando, W. A. (1988). "Processing And Use Of Zirconium Based Materials." In *Advanced Materials and Manufacturing Processes* (Vol. 3, Issue 2, pp. 195–231). https://doi.org/10.1080/10426918808953203

Ferreira, F. (2017). "Process-Properties Relations in Deep Oscillation Magnetron Sputtering." Doctoral thesis in Mechanical Engineering, Surface Engineering, Mechanical Engineering Department, University of Coimbra.

Ferreira, F., Oliveira, J. C., & Cavaleiro, A. (2016). "CrN thin films deposited by HiPIMS in DOMS mode." *Surface and Coatings Technology*, *291*, 365–375. https://doi.org/10.1016/j.surfcoat.2016.02.064

Ferreira, F., Serra, R., Cavaleiro, A., & Oliveira, J. C. (2016). "Additional control of bombardment by deep oscillation magnetron sputtering: Effect on the microstructure and topography of Cr thin films." *Thin Solid Films*, *619*, 250–260. https://doi.org/10.1016/j.tsf.2016.10.054

Ferreira, F., Serra, R., Oliveira, J. C., & Cavaleiro, A. (2014). "Effect of peak target power on the properties of Cr thin films sputtered by HiPIMS in deep oscillation magnetron sputtering (DOMS) mode." *Surface and Coatings Technology*, *258*, 249–256. https://doi.org/10.1016/j.surfcoat.2014.09.020

Hajihoseini, H., Kateb, M., Ingvarsson, S., & Gudmundsson, J. T. (2018). "Effect of substrate bias on properties of HiPIMS deposited vanadium nitride films." *Thin Solid Films*, *663*, 126–130. https://doi.org/10.1016/j.tsf.2018.06.060

J V Menghani 1, K.B Pai 2, M.K Totlani 3, & N Jalgoankar 4. (2018, January 8). "Investigation on Corrosion Behaviour of ZrN Thin Films in Industrial Environment." https://doi.org/10.15242/dirpub.dir1017014

Kelly, P. J., & Arnell, R. D. (n.d.). "Magnetron sputtering: a review of recent developments and applications."

Kuznetsova, T., Lapitskaya, V., Khabarava, A., Chizhik, S., Warcholinski, B., & Gilewicz, A. (2020). "The influence of nitrogen on the morphology of ZrN coatings deposited by magnetron sputtering." *Applied Surface Science*, *522*. https://doi.org/10.1016/j.apsusc.2020.146508

Laurentiu, M., Lidia, B., Eliza, D., & Valentin, D. (2016). "Polymeric coatings used against marine corrosion of naval steel EN32." *Key Engineering Materials*, *699*, 71–79. https://doi.org/10.4028/www.scientific.net/KEM.699.71

Li, B. S., Wang, T. G., Ding, J., Cai, Y., Shi, J., & Zhang, X. (2018). "Influence of N2/Ar flow ratio on microstructure and properties of the AlCrSiN coatings deposited by

high-power impulse magnetron sputtering." *Coatings*, *8*(1). https://doi.org/10.3390/coatings8010003

Maculotti, G., Genta, G., Quagliotti, D., Galetto, M., & Hansen, H. N. (2022). "Gaussian process regression-based detection and correction of disturbances in surface topography measurements." *Quality and Reliability Engineering International*, *38*(3), 1501–1518. https://doi.org/10.1002/qre.2980

Mejía, C. P., Vanegas, H. S., & Olaya, J. J. (2022). "Electrochemical and Optical Behavior of ZrN-Ag Coatings Deposited by Means of DC Reactive Magnetron Sputtering Technique." *Coatings*, *12*(6), 754. https://doi.org/10.3390/coatings12060754

Milosev, I., Strehbtow, H.-H., & Navin~ek, B. (1997). "Comparison of TiN, ZrN and CrN hard nitride coatings: Electrochemical and thermal oxidation." In *Thin Solid Films* (Vol. 303).

Mu, S., Liu, J., Lin, W., Wang, Y., Liu, J., Shi, L., & Jiang, Q. (2017). "Property and microstructure of aluminosilicate inorganic coating for concrete: Role of water to solid ratio." *Construction and Building Materials*, *148*, 846–856. https://doi.org/10.1016/j.conbuildmat.2017.05.070

Musil, J., Zenkin, S., Kos, Čerstvý, R., & Haviar, S. (2016). "Flexible hydrophobic ZrN nitride films." *Vacuum*, *131*, 34–38. https://doi.org/10.1016/j.vacuum.2016.05.020

Oliveira, J. C., Fernandes, F., Ferreira, F., & Cavaleiro, A. (2015). "Tailoring the nanostructure of Ti-Si-N thin films by HiPIMS in deep oscillation magnetron sputtering (DOMS) mode." *Surface and Coatings Technology*, *264*, 140–149. https://doi.org/10.1016/j.surfcoat.2014.12.065

Pejaković, V., Totolin, V., Göcerler, H., Brenner, J., & Rodríguez Ripoll, M. (2015). "Friction and wear behaviour of selected titanium and zirconium based nitride coatings in Na2SO4 aqueous solution under low contact pressure." *Tribology International*, *91*, 267–273. https://doi.org/10.1016/j.triboint.2015.04.047

Pistone, A., Scolaro, C., & Visco, A. (2021a). "Mechanical properties of protective coatings against marine fouling: A review." In *Polymers* (Vol. 13, Issue 2, pp. 1–19). MDPI AG. https://doi.org/10.3390/polym13020173

Purandare, Y., Ehiasarian, A., Santana, A., & Hovsepian, P. (2014). "ZrN coatings deposited by high power impulse magnetron sputtering and cathodic arc techniques." *Journal of Vacuum Science & Technology A: Vacuum, Surfaces, and Films*, *32*(3), 031507. https://doi.org/10.1116/1.4869975

Purandare, Y. P., Ehiasarian, A. P., & Hovsepian, P. Eh. (2011). "Structure and properties of ZrN coatings deposited by high power impulse magnetron sputtering technology." *Journal of Vacuum Science & Technology A: Vacuum, Surfaces, and Films*, *29*(1), 011004. https://doi.org/10.1116/1.3520640

Ramsey, P. M., Chandler, H. W., & Page, T. F. (1990). "The determination of residual stresses in thin coatings by a sample thinning method." In *Surface and Coatings Technology* (Vol. 43).

Rebelo, R., Manninen, N. K., Fialho, L., Henriques, M., & Carvalho, S. (2016). "Morphology and oxygen incorporation effect on antimicrobial activity of silver thin films." *Applied Surface Science*, *371*, 1–8. https://doi.org/10.1016/j.apsusc.2016.02.148

Shiri, S., Ashtijoo, P., Odeshi, A., & Yang, Q. (2016). "Evaluation of Stoney equation for determining the internal stress of DLC thin films using an optical profiler."

Surface and Coatings Technology, *308*, 98–100. https://doi.org/10.1016/j.surfcoat.2016.07.098

Strijckmans, K., Schelfhout, R., & Depla, D. (2018). "Tutorial: Hysteresis during the reactive magnetron sputtering process." *Journal of Applied Physics*, *124*(24). https://doi.org/10.1063/1.5042084

Tang, J. F., Lin, C. Y., Yang, F. C., Tsai, Y. J., & Chang, C. L. (2020). "Effects of nitrogen-argon flow ratio on the microstructural and mechanical properties of AlCrN coatings prepared using high power impulse magnetron sputtering." *Surface and Coatings Technology*, *386*. https://doi.org/10.1016/j.surfcoat.2020.125484

Ulaeto, S. B., Rajan, R., Pancrecious, J. K., Rajan, T. P. D., & Pai, B. C. (2017). "Developments in smart anticorrosive coatings with multifunctional characteristics." In *Progress in Organic Coatings* (Vol. 111, pp. 294–314). Elsevier B.V. https://doi.org/10.1016/j.porgcoat.2017.06.013

Wood, K., Puget, Y., Tretheweyb, K. R., & Stokes, K. (1998). "The performance of marine coatings and pipe materials under fluid-borne sand erosion." In *Wear* (Vol. 219). ELSEVIER.

Yi, P., Zhu, L., Dong, C., & Xiao, K. (2019). "Corrosion and interfacial contact resistance of 316L stainless steel coated with magnetron sputtered ZrN and TiN in the simulated cathodic environment of a proton-exchange membrane fuel cell." *Surface and Coatings Technology*, *363*, 198–202. https://doi.org/10.1016/j.surfcoat.2019.02.027

Zhang, J. J., Wang, M. X., Yang, J., Liu, Q. X., & Li, D. J. (2007). "Enhancing mechanical and tribological performance of multilayered CrN/ZrN coatings." *Surface and Coatings Technology*, *201*(9-11 SPEC. ISS.), 5186–5189. https://doi.org/10.1016/j.surfcoat.2006.07.093

Zhang, Y., Chen, F., Zhang, Y., Liu, M., Pang, Y., Yan, J., & Du, C. (2022). "Corrosion and tribocorrosion behaviors of ternary TiZrN coating on 304 stainless steel prepared by HiPIMS." *Materials Today Communications*, *31*. https://doi.org/10.1016/j.mtcomm.2022.103258